EUROPEAN ORGANISATION FOR NUCLEAR RESEARCH

OPAL – PRNNN Updated Draft 2
July 2th, 2004

# Determination of $\alpha_s$ using Jet Rates at LEP with the OPAL Detector

The OPAL Collaboration

**Abstract:**
Hadronic events produced in $e^+e^-$ collisions by the LEP collider and recorded by the OPAL detector were used to form distributions based on the number of reconstructed jets. The data were collected between 1995 and 2000 and nd correspond to energies of 91 GeV, 130-136 GeV and 161-209 GeV. The jet rates are determined using four different jet finding algorithms. The differential two-jet rate and the average jet rate with the Durham and Cambridge algorithms are used to measure $\alpha_s$ in the LEP energy range by fitting an expression in which $\mathcal{O}(\alpha_s^2)$ calculations are matched to a NLLA prediction to the data. Combining the measurements at different centre-of-mass energies the value of $\alpha_s(M_{Z^0})$ is determined to be

$$\alpha_s(M_{Z^0}) = 0.1197 \pm 0.0010(\text{stat.}) \pm 0.0012(\text{expt.}) \pm 0.0021(\text{had.}) \pm 0.0033(\text{theo.}).$$

Author:
Michael Donkers

Editorial Board:
Andreas Ludwig, Isabel Trigger, Stefan Kluth and Zoltán Trócsányi

# 1 Introduction

In the Standard Model of elementary particle interactions, the strong interaction is described by the theory of Quantum Chromodynamics (QCD), and depends on just one fundamental parameter, the strong coupling $\alpha_s$. Th Dispatch 1863

e value of $\alpha_s$ is expected to depend on the energy scale of the interaction. It is therefore an important test of the theory to determine the value of $\alpha_s$ experimentally at as many different energies using as many different techniques as possible. footnote 1: "The right-handed OPAL coordinate system... "

Indeed, many methods have already been employed to evaluate the value of $\alpha_s$. At very low energies the value of $\alpha_s$ can be measured using the hadronic decays of the $\tau$ lepton [1] and heavy quarkonia [2]. Low energy determinations are also available using scaling violations [3, 4] and sum rules [5, 6] from deep inelastic scattering experiments. Higher energy determinations of $\alpha_s$ come from collider experiments ($e^+e^-$, pp, $p\bar{p}$, or ep) using properties of the created hadron system which are explicitly dependent on the value of $\alpha_s(\sqrt{s})$, where $\sqrt{s}$ corresponds energy scale at which the interaction takes place.

During the LEP1.5 and LEP2 operational phases of the Large Electron-Positron collider at CERN events were recorded with centre-of-mass collision energies ranging from 91 GeV to 209 GeV. Events of the form $e^+e^- \rightarrow$hadrons can be used to determine distributions based on the ensemble of final state hadrons (event shapes) or on the ensemble of jets (jet rates). Previous results by OPAL for an $\alpha_s$ determination based on event shapes and jet rates using the $Z^0$ dataset collected during the LEP1 phase can be found in [7]. Determinations of $\alpha_s$ from LEP1.5 and LEP2 datasets up to 189 GeV have already been reported by OPAL based on event shape distributions [8, 9, 10] and on jet rates [11].

Tha analysis presented in this paper we used data collected during the LEP1.5 and LEP2 phases to construct jet rate distributions using several jet clustering algorithms. The differential two-jet rate, $D_2$, and the average jet rate, $\langle N \rangle$, were used to determine values of $\alpha_s$ ($\sqrt{s}$) at the 4 combined centre-of-mass energies comprised of data within the LEP1.5 and LEP2 datasets. Theoretical predictions were fitted to these distributions to extract the value of $\alpha_s(\sqrt{s})$.

The paper is organised as follows. Section 2 contains a brief description of the OPAL detector. A summary of the data and the Monte Carlo samples used in the analysis, together with the methods used to select signal events and reject backgrounds, is given in Section 3. In section 4 we define the jet rate distributions. Finally, the results of this analysis are given in Section 5, followed by a conclusion and summary in Section 6.

# 2 The OPAL Experiment

A full description of the OPAL detector can be found in [12]. The critical components of the detector in the identification of jets were the central tracking chambers, which were used to reconstruct charged particles, and the electromagnetic and hadronic calorimeters, which measured the total energy deposited by charged and neutral particles.

The tracking chambers were located inside a solenoidal magnet which provided a 0.435 T axial magnetic field along the beam axis. The main component of the tracking system was

a large volume jet chamber, which was approximately 4.0 m long with an outer radius of 1.85 m. The jet chamber was separated into 24 sectors each with a radial plane of 159 sense wires separated by 1 cm. The momenta of tracks in the $x-y$ [1] plane were measured with a precision parametrized by $\sigma_p/p = \sqrt{0.02^2 + (0.0015 \cdot p[\mathrm{GeV}/c])^2}$.

The calorimetry systems were outside the solenoidal magnet. The electromagnetic calorimeter was composed of 11704 lead glass blocks in the barrel and endcap regions, representing about 25 radiation lengths in the barrel and more than 22 in the endcap. The iron sampling hadron calorimeter was located just outside the electromagnetic calorimeter, and provided the stopping power to contain all hadronic showers. Luminosity was determined using small-angle Bhabha events detected in the forward detectors and silicon-tungsten calorimeter [13].

Data from most of the subdetectors were collected after an event had been triggered [14], and processed by the OPAL data acquisition system [15]. The raw event data were transferred to a farm of computer processors where the events were fully reconstructed and written to tape for offline analysis.

## 3 Data Samples and Event Selection

The data used in this analysis were collected by OPAL between 1995 and 2000 and correspond to integrated luminosities of 14.5 $\mathrm{pb}^{-1}$ of 91 GeV data, 11.3 $\mathrm{pb}^{-1}$ of LEP1.5 data with centre-of-mass energies between 130 GeV and 136 GeV and 707.4 $\mathrm{pb}^{-1}$ of LEP2 data with centre-of-mass energies ranging from 161 to 209 GeV. The 91 GeV data, known as $\mathrm{Z}^0$-calibration data, were primarily collected for calibrating parameters used in the OPAL reconstruction algorithms. This $M_{\mathrm{Z}^0}$ sample had the same detector configuration as the other centre-of-mass engery points. The exact breakdown of the centre-of-mass energies together with the respective luminosities and numbers of selected events are given in Table 1. The thirteen points in Table 1 represent the main samples of the spread of energies in the LEP1.5 and LEP2 data.

The LEP1.5 and LEP2 data were combined into four datasets within separate energy regions by taking a suitably weighted average of the individual samples. The LEP1.5 dataset provided a single energy point at a luminosity-weighted centre-of-mass energy of 133 GeV, while the LEP2 datasets were split into two energy points, one with a luminosity-weighted centre-of-mass energy of 179 GeV using data in the range 161 – 183 GeV (with a total integrated luminosity of 78.1 $\mathrm{pb}^{-1}$) and another at 198 GeV (with a total integrated luminosity of 628.3 $\mathrm{pb}^{-1}$) using data in the range 189 – 209 GeV. Together with the $\mathrm{Z}^0$-calibration data this provided for a determination of $\alpha_{\mathrm{s}}$ at four separate centre-of-mass energies.

### 3.1 Monte Carlo Samples

A number of Monte Carlo samples were created to correct for detector acceptance and resolution effects, to correct for hadronization effects and to estimate the contribution of background processes. These Monte Carlo sample were produced using a full simulation of the

[1] The right-handed OPAL coordinate system is defined so that $z$ is the coordinate parallel to the $\mathrm{e}^-$ beam direction and the $x$ axis points to the centre of the LEP ring, the $r$ direction is normal to the $z$ axis, $\theta$ is the polar angle with respect to the $z$ axis and $\phi$ is the azimuthal angle with respect to the $x$ axis

detector [16], followed by the same reconstruction and selection algorithms as applied to the real data, and are referred to as "detector level" samples. Other samples without the full detector simulation are discussed in Section 3.3

PYTHIA 6.150 [17] was used to provide the default Monte Carlo samples (for the process $e^+e^- \to Z/\gamma^* \to q\overline{q} \to$ hadrons) which were used to correct the high energy datasets. The $Z^0$-calibration dataset was corrected using JETSET 7.408 [18]. Hadronization corrections were evaluated by comparing results with alternative an Monte Carlo sample. The HERWIG 6.2 [19] Monte Carlo uses the cluster model of hadronization. This was compared with the string model of hadronization in PYTHIA. Parameters involved in the Monte Carlo simulation, both for JETSET/PYTHIA and HERWIG, were tuned to OPAL data collected at the $Z^0$ peak, including global event shapes, particle multiplicities and fragmentation functions [20, 21]. The generation of the initial quark-antiquark pair, for each Monte Carlo sample, was implemented using the $\mathcal{KK}$2f 4.14 event generator [22] which has an improved description of photon production in the initial and final states than currently implemented in the PYTHIA generator. The available detector level Monte Carlo samples are listed in Table 1.

Above the $W^+W^-$ production threshold (161 GeV), the main background was expected to come from four-fermion events, in particular those events in which two or all four of the fermions are quarks. The contribution of these backgroundsin data was estimated using Monte Carlo samples generated using KORALW 1.42 [23] (for $q\bar{q}q'\bar{q}'$ and $q\bar{q}\ell\bar{\ell}^{(\prime)}$ where $\ell = e, \mu, \tau, \nu$ but $\ell\bar{\ell} \neq e^+e^-$) and grc4f 2.1 [24] (for $eeq\bar{q}$). Grc4f 2.1 was used to generate all the expected four-fermion background samples for the 161 and 172 GeV data. The background distributions were normalized to the luminosity of the dataset and subsequently subtracted from the measured distributions. The LEP1.5 energies were well below the $W^+W^-$ and $Z^0Z^0$ production thresholds [25] and were therefore expected to have no significant four-fermion backgrounds. The total expected background contribution from $e^+e^- \to q\overline{q}q\overline{q}$ events is 1.2% of the combined LEP1.5 data sample and it was neglected in the analysis.

### 3.2 Selection Method

**Preselection**

All events within a dataset were required to contain information from both the central jet chamber and the electromagnetic calorimeter, meaning both these subdetectors must have been flagged as being on and in good operational condition. In addition events were required to be tagged as multihadronic in order to be selected for analysis. Multihadronic events were identified using the criteria described in [26] for events with $\sqrt{s} > M_{Z^0}$ and in [27] for $Z^0$-calibration events. An event was required to contain at least seven good tracks to reduce potential backgrounds arising from the production of $\tau$ leptons ($e^+e^- \to \tau^+\tau^-$) decaying into hadrons and from two photon interactions producing quarks. Good tracks were defined as those which had

- at least 40 hits in the jet chamber
- at least 150 MeV/$c$ transverse momentum relative to the beam axis.

- the distance of closest approach to the interaction point in the $r - \phi$ plane satisfying $d_0 \leq 2$ cm
- the distance of closest approach to the interaction point in the $r - z$ plane satisfying $|z_0| \leq 25$ cm.

Events which met the detector status requirements, were tagged as multihadronic, and contained at least seven reconstructed good tracks then passed preselection.

All of the good quality tracks and clusters in the event were used to define "objects" representing particles using an algorithm to correct for double counting of energy. This matching and compensation process, termed the MT algorithm [28, 29] produced a uniquely defined array of track and cluster objects. The trajectories of the tracks measured in the central tracking chambers were extrapolated to the clusters in the electromagnetic and hadronic calorimeters. If a spatial association was established, then the track momentum and cluster energy were compared. If the energy of the cluster was less than expected from the track, then the cluster was omitted to avoid double counting of energy, since the momentum resolution for tracks was typically better than the calorimeter energy resolution. If the energy of the cluster was larger than expected the energy of the cluster was reduced by the expected amount with the remaining energy interpreted as due to photons or neutral hadrons. These remaining clusters and those which were not matched defined the four-vectors of "neutral" particles.

**Containment**

We ensured that most particles in the event are well contained in the detector and not lost down the beam line by imposing a cut on the direction of the thrust axis [30],

- $|\cos\theta_{\rm T}| < 0.9$,

where $\theta_{\rm T}$ is the angle between the beam axis and the direction of the thrust axis. Note the thrust axis direction was determined from all tracks and clusters in the event, without correcting for double counting with the MT algorithm.

**Initial State Radiation (ISR) Cuts**

The events of interest for this analysis were $e^+e^- \rightarrow q\overline{q}$ events where final state $q\overline{q}$ pair has the full centre-of-mass energy. The effective centre-of-mass energy of the e+e- collision can be reduced by the emission of one or more ISR photons. At LEP2, approximately three quarters of the multihadronic events are such radiative return events, where the invariant mass of the qqbar pair is close to the $Z^0$ mass. The effective centre-of-mass energy of the collision, $\sqrt{s'}$ [31], was evaluated, and the requirement,

- $\sqrt{s} - \sqrt{s'} < 10$ GeV

was imposed to select full energy events.

To calculate rootsprime, all isolated photon candidates with energies greater than 10 GeV were identified. The Durham jet reconstruction algorithm [31] was then used to group the remaining tracks and clusters into jets. ISR photons are often emitted close to the beam direction. Three kinematic fits were performed, under the assumptions that

- there were two undetected photons (in opposite directions along the beam pipe)
- there was one undetected photon
- all photons were observed in the detector.

The fit with the most acceptable chisquared was selected, and $\sqrt{s'}$ was calculated from the invariant mass of the jets, excluding any photons.

The power of this cut can be seen in Figure 1. The efficiency for selecting non-radiative qqbar events is given in Table 2. Non-radiative $q\overline{q}$ events are defined as those in which $\sqrt{s}$-$\sqrt{s'_{\rm true}}$ <1 GeV, where $s'_{\rm true}$ is determined from generator level information in the PYTHIA samples. This ISR is applied to all analyzed datasets with the exception of the $Z^0$ calibration data.

**Final Cuts**

The dominant background to the process $e^+e^- \rightarrow Z/\gamma^* \rightarrow q\overline{q} \rightarrow$ hadrons comes from the four-fermion process $e^+e^- \rightarrow W^+W^-$ in which one or both of the bosons decay hadronically, producing two or four quarks in the final state. This background was expected to make up approximately 30% of all observed events in each of the LEP2 datasets which pass the first stage of cuts. These backgrounds were addressed by [32] placing a cut on two likelihood values which indicate how likely an event is to be a non-QCD four-quark or a semi-leptonic event:

- $\mathcal{L}_{\rm qqqq} < 0.25$
- $\mathcal{L}_{\rm qq\ell\nu} < 0.50$

The effect of these cuts in each of the LEP2 datasets and the expected backgrounds can be seen on Figure 2.

The four-quark likelihood value [33], $\mathcal{L}_{\rm qqqq}$, was estimated from four kinematic variables describing characteristics of hadronic $W^+W^-$ decays like their four-jet nature and angular structure. These variables were used to construct event probabilities based on two hypotheses: first, that the event was due to a hadronically decaying $W^+W^-$ pair ($W^+W^- \rightarrow q\overline{q}q\overline{q}$) and, second, that the event was due to a hadronically decaying $Z/\gamma^*$ ($e^+e^- \rightarrow Z/\gamma^* \rightarrow q\overline{q}$). The probabilities were combined to produce the discriminating likelihood, $\mathcal{L}_{\rm qqqq}$. This cut reduced the expected background by approximately 80% so that it constitutes only 9% of the observed number of events.

The semi-leptonic likelihood [33], $\mathcal{L}_{\rm qq\ell\nu}$, was based upon three separate likelihoods, one for each lepton species ($\ell$ =e, $\mu$, $\tau$). Each of these likelihoods was based on ten variables describing the properties of the lepton, the jets produced by the $q\overline{q}$ pair and the missing energy carried away by the neutrino. This cut in conjunction with the cut on the four-quark likelihood removed almost 90% of the background expected in the observed LEP2 dataset. The effect of these cuts can be seen in Figure 2.

These likelihood cuts also reduce the backgrounds arising from $e^+e^- \rightarrow Z^0Z^0$ in which one or both of the $Z^0$ bosons decay hadronically. This backgroundWhat do you mean by 'detector conditions ... were varied'? was much smaller because the cross-section of $Z^0Z^0$ production is

much smaller than that of $W^+W^-$ production. The likelihood cuts are applied to only those datasets with $\sqrt{s}$ $\geq$161 GeV.

The expected size of the total background contribution to each dataset was determined by Monte Carlo predictions after scaling to the luminosity of the dataset. The effect of the final cuts and the expected four-fermion backgrounds for each centre-of-mass energy dataset can be seen in Table 2. As seen in the table the likelihood cuts greatly increase the purity of selected non-radiative $q\overline{q}$ events. The LEP2 datasets are typically $\approx$70% pure following the ISR rejection; however, after the likelihood cuts this jumps to a purity of 93-95%.

### 3.3 Monte Carlo Corrections

The background rejection cut does not remove all of the expected backgrounds from $W^+W^-$ and $Z^0Z^0$ production. The remaining backgrounds, taken from the Monte Carlo, were subtracted from the corresponding measured distributions on a bin-by-bin basis. Uncertainties in this procedure will be discussed in Section 6.

Corrections to the distributions were also made for effects arising from finite detector resolution and a limited detector acceptance (recall that the event quality cut on $|\cos\theta_{\rm T}|$ will reduce the fiducial volume) and for residual ISR events which were not removed by the $\sqrt{s'}$ cut. These corrections were accomplished by comparing distributions from two separate Monte Carlo samples, one of which had gone through a full detector simulation, including effects of detector resolution and acceptance and initial state radiation, called the "detector" level. The other sample used only the generator-level hadrons and had not gone through the detailed detector simulation. In this sample all short-lived particles ($\tau \leq 3 \times 10^{-10}$s) had decayed and a requirement that $\sqrt{s} - \sqrt{s'_{\rm true}}$ <1 GeV was imposed. This "hadron level" sample was thus expected to produce distributions arising solely from the properties of the underlying hadrons, free of any detector biases determined over the full acceptance without any limitations arising from limited resolution.

Correction factors for each bin of the distributions were determined from the ratio of the two Monte Carlo distributions. Thus, any bin, $i$, of the measured distributions was corrected via

$$\mathcal{H}_i^{\rm data} = \left(\frac{\mathcal{H}_i^{\rm MC}}{\mathcal{D}_i^{\rm MC}}\right)(\mathcal{D}_i^{\rm data} - \mathcal{D}_i^{\rm bkgd}) \qquad (1)$$

where $\mathcal{H}$ and $\mathcal{D}$ represent distributions at the hadron level and the detector level respectively, and $\mathcal{D}_i^{\rm bkgd}$ corresponds to the expected size of the total background in bin $i$. The hadron level was used in this analysis when determining jet rate distributions; however, the theoretical predictions which were fitted to these distributions were obtained from computations valid at the "parton level". The parton level corresponds to distributions that would be produced if only the partons created immediately following the $e^+e^-$ annihilation and before the hadronization phase are used in the analysis. The parton level Monte Carlo sample is built from quarks and gluons that are produced during the parton cascade simulated by the generator before the hadronization phase begins. As in the case of the hadron level, the parton level sample gave rise to distributions that were free of initial state radiation without any detector simulation applied. The correction factor determined from the ratio of the hadron level to the parton level was applied to the theoretical predictions before the fitting procedure.

This factor corrected the prediction to the hadron level so that it could be compared to the corrected hadron level distribution determined from the data,

$$\mathcal{H}_i^{\mathrm{pred}} = \left( \frac{\mathcal{H}_i^{\mathrm{MC}}}{\mathcal{P}_i^{\mathrm{MC}}} \right) \mathcal{P}_i^{\mathrm{pred}} \tag{2}$$

where $\mathcal{H}$ and $\mathcal{P}$ represent distributions at the hadron level and the parton level respectively.

## 4 Jet Rate Distributions

Jets were formed from the final state objects by applying jet clustering algorithms. These algorithms use the kinematic and spatial (geometric) properties of the individual objects in order to classify them as belonging to a specific jet. We used here the Durham [34], Cambridge [35], JADE [36] and the $R$ and $\varepsilon$ variants of the CONE [37] jet clustering algorithms.

The Durham and Cambridge algorithms construct a test variable built from the energy and angular separation between two particles,

$$y_{ij} = \frac{2 \min\{E_i^2, E_j^2\}(1 - \cos\theta_{ij})}{E_{\mathrm{vis}}^2}$$

where $E_i$ is the energy of particle $i$, $\theta_{ij}$ the angle between the particle $i$ and $j$ and $E_{\mathrm{vis}}$ is the total visible energy in the event. The pair that produces the smallest value of $y_{ij}$ is chosen first. The value of this test variable is compared to a predefined parameter, $y_{\mathrm{cut}}$, called the jet resolution parameter. If the test variable is smaller than $y_{\mathrm{cut}}$ the particles are merged into a pseudo-particle by adding their four-momenta and the test variable is formed with again other particles. Should the test variable be larger than $y_{\mathrm{cut}}$, the (pseudo-)particles $i$ and $j$ are considered to constitute a jet, and are removed from this list of eligible particles for jet formation. The smallest test variable is then constructed again using particles not already assigned to a jet, and compared to $y_{\mathrm{cut}}$. This process continues until all particles in the event are assigned to jets.

The Cambridge algorithm differs slightly from Durham in its implementation. In the Cambridge algorithm particles are first paired together by minimising the variable $v_{ij} = 2(1 - \cos\theta_i j)$. The standard test variable is then constructed and compared to the jet resolution parameter, $y_{\mathrm{cut}}$. The procedure followed is then identical to that of the Durham algorithm, except that only the lowest energy (pseudo)particle is taken as the jet when $y_{ij} > y_{\mathrm{cut}}$. The number of jets reconstructed in the event, using Durham or Cambridge, is therefore a function of the jet resolution parameter. The JADE algorithm follows the same procedure as the Durham algorithm; however, it uses the scaled invariant mass, $y_{ij} = 2E_iE_j(1 - \cos\theta_{ij})/E_{\mathrm{vis}}^2$, of particles $i$ and $j$ as the test variable.

In the Cone jet finding algorithm, a jet is defined as a set of particles whose three-momentum vectors lie inside a cone of half angle $R$, where the direction of the sum of their three-momentum vectors defines the cone axis. In addition, the total energy of the particles assigned to a jet is required to exceed some minimum value $\varepsilon$. Typical values are $R = 0.7$ rad and $\varepsilon = 7$ GeV for jets in $e^+e^-$ annihilation at LEP 1 energies. When analysing events at the detector level, we replaced $\varepsilon$ by $\varepsilon' = \varepsilon \cdot E_{\mathrm{vis}}/\sqrt{s}$ to compensate for the incomplete detection

of the energy of the event. In our studies, the jet rate was computed at fixed $\varepsilon = 7$ GeV as $R$ was varied, and at fixed $R = 0.7$ as $\varepsilon$ was varied. The former is sensitive to the angular structure of jets, and the latter to their energy distribution.

The fraction of multihadronic events in a given sample that are classified as containing $n$ jets for a given value of the jet resolution parameter ($y_{\rm cut}$, $R$ or $\varepsilon$) is referred to as the $n$-jet rate. This $n$-jet rate is explicitly defined as

$$R_n(y_{\rm cut}) = \frac{\sigma_n(y_{\rm cut})}{\sigma_{\rm tot}} \equiv \frac{N_n(y_{\rm cut})}{N_{\rm tot}}, \tag{3}$$

where $\sigma_n$ is the cross-section for the production of a hadronic event with $n$ jets at fixed $y_{\rm cut}$, $\sigma_{tot}$ is the total hadronic cross-section, $N_n(y_{\rm cut})$ is the number of events in a sample with $n$ jets for a given value of $y_{\rm cut}$ and $N_{tot}$ is the total number of events in that sample.

The differential $n$-jet rate was also determined. It the derivative of the $n$-jet rate with respect to $y_{\rm cut}$,

$$D_n(y_{\rm cut}) \;=\; \frac{{\rm dR_n}(y_{\rm cut})}{{\rm d}y_{\rm cut}}. \tag{4}$$

For the case when $n = 2$, the differential 2-jet rate reduces to $D_2 = y_2$, where $y_2$ is the value of the jet resolution parameter where the event flips from a 2- to a 3-jet event. When using the Durham algorithm to define jets the value of $D_2$ (denoted $y_{23}^D$) is also an event shape variable.

The average number of jets per event in a given sample, as a function of the jet resolution parameter, is defined to be

$$\langle N \rangle(y_{\rm cut}) \;=\; \frac{1}{\sigma_{\rm tot}} \sum_n n\sigma_n(y_{\rm cut}) \tag{5}$$

$$\;=\; \frac{1}{N_{tot}} \sum_n n N_n(y_{\rm cut}). \tag{6}$$

In the subsequent analysis, the differential and average jet rates have been determined using the Durham and Cambridge clustering algorithms, since the resummed predictions only exist for these algorithms. This then provided four separate observables ($D_2^D$, $D_2^C$, $\langle N \rangle^D$ and $\langle N \rangle^C$) which were used to determine a value of $\alpha_{\rm s}$ at the four different centre-of-mass energy values. A $\ln R$ matched prediction, as described in Appendix A, was fit to the distributions from the four observables.

# 5 Systematic Studies

## 5.1 Experimental Systematic Variations

Several selection algorithms and selection cuts were varied to determine their systematic impact on the results of the analysis. In all cases the result from the variation was compared to the result from the standard selection, the difference was then taken as a contribution total systematic error.

**Tracking** Systematic errors relevant to the definition of objects defined within the tracking chambers and calorimeters, and hence used for jet clustering, were estimated by comparing the results using the MT package to an alternative method of defining tracks. This alternative method used all selected tracks and clusters without taking into account the possibility of double counting.

**Containment** The constraint on the direction of the thrust axis was tightened to $|\cos\theta_T| < 0.7$, restricting events to the barrel region.

**$\mathcal{L}_{\mathrm{qqqq}}$ and $\mathcal{L}_{\mathrm{qq}\ell\nu}$** To account for the systematic uncertainty that arises from the value of the cut placed on the $\mathrm{W^+W^-}$ hadronic and semi-leptonic likelihoods, the values of the likelihood cuts were changed to 0.1 and 0.4 for $\mathcal{L}_{\mathrm{qqqq}}$ and to 0.25 and 0.75 for $\mathcal{L}_{\mathrm{qq}\ell\nu}$. In each case the largest variation is taken.

**Backgrounds** To account for uncertainties introduced during background subtraction, arising from imprecise knowledge of the four-fermion cross-sections, these cross-sections were conservatively varied by $\pm 5\%$ and the largest deviation from the standard value was used to determine an overall systematic error.

**ISR** A possible systematic effect introduced through the selection of events with little or no initial state radiation was estimated by repeating the selection using a second method of ISR determination [38]. This alternative method assumed while performing the kinematic fit that there was always a single photon which either escaped undetected down the beam line or was detected in the electromagnetic calorimeter.

**Detector Correction** The uncertainty in modelling the detector was investigated by using HERWIG Monte Carlo datasets in place of PYTHIA to correct from the detector level to the hadron level. The hadronization correction was still performed using the PYTHIA Monte Carlo samples.

### 5.2 Hadronization Systematic Variations

Systematic uncertainties could arise from the modelling of the hadronization. These were estimated by using HERWIG Monte Carlo samples, which employ a different hadronization model. The PYTHIA-HERWIG differences were taken to be the systematic uncertainties from hadronization.

### 5.3 Theoretical Systematic Variations

Three further systematic variations were considered when fitting the data for a determination of $\alpha_{\mathrm{s}}$.

**Fit Range** We investigate the choice of the range of bins used in performing the fit of the theoretical prediction to the data (see Section 6.2). The fit range was first increased by two bins, by adding one bin to each endpoint of the fit range. In the case where one of the endpoints was already at the maximum allowed bin value, only the other point was extended by one bin. A second variation decreased the fit range by two bins, by

removing a bin from each endpoint of the fit range. The largest deviation from the standard fit value was taken as the contribution to the systematic error.

**Renormalization Scale** The second fit-related systematic variation accounts for the uncertainty due to the renormalization scale, $x_\mu$, dependence of the fixed order and resummed predictions, where $x_\mu = \mu/sqrts$. The value of $x_\mu$, which was set to 1.0 in the standard fits, was varied to 0.5 and 2.0 respectively. The largest deviation from the standard fit value was taken as the contribution to the systematic error representing renormalization scale uncertainty.

**Logarithm rescaling, $x_L$** In the resummation process for event shape variables, like $D_2$, there is an arbitrariness due to the definition of the logarithms which are resummed. In this analysis we have used $\alpha_s \ln(1/y_{\rm cut})$; however, this could be generalized to powers of $\alpha_s \ln[1/(x_L\, y_{\rm cut})]$ [39]. The standard value for this rescaling ($x_L$=1) was varied to $\frac{4}{9}$ and $\frac{9}{4}$, to investigate the systematic effect of this arbitrariness. There is no similar rescaling definition for the case of the average jet rates, so the $x_L$ variations are only shown for the $D_2$ distributions for comparison to the $x_\mu$ variation. [2] Hence this variation was not used in the determination of the total theoretical systematic error. A comprehensive study of the combination of various theoretical variations to produce a global theoretical uncertainty for event shape distributions is given in [40].

The differences between the standard result and those due to the above variations were separated into three categories, experimental, hadronization and theory (see Table 3). The variations in each of these categories were added in quadrature and the result taken as the systematic uncertainty for that category. In the case of asymmetric errors, the error was symmetrized by taking the largest systematic variation and applying it as the full systematic contribution. A summary of the systematic variations is provided in Table 3.

## 6 Results

Data from thirteen separate datasets were used were used in this analysis, one $Z^0$-calibration dataset, two LEP1.5 datasets and ten datasets from LEP2. These thirteen datasets were combined to produce four higher statistics datasets ($\sqrt{s}$ =$M_{Z^0}$, 133, 178 and 198 GeV) which were analysed separately. The raw distributions ($n$-jet fractions, $D_2$ and $\langle N \rangle$) for each of the datasets were determined as functions of the jet resolution parameters defined using five different jet clustering algorithms. The distributions underwent a bin-by-bin correction which included subtraction of expected backgrounds and correction for detector and residual ISR effects. Systematic effects were examined by varying the parameters used in selecting events (see Table 3). The difference between the corrected distributions using these variations and those from the standard selection then determined the size of the systematic error on each bin of the distribution.

[2] Variations from $x_L$ are not made in addition to but in combination with $x_\mu$, i.e. the larger of the two taken as the systematic error. The treatment in [40] is to produce an error band based upon several theoretical systematic variations. In general the size of the error band is closely approximated over the fit range used in this analysis by taking the largest $x_\mu$ variation as the contribution to the theoretical error.

The corrected $D_2$ and $\langle N \rangle$ distributions were fitted to Durham and Cambridge ln $R$ matching predictions over a predetermined fit range, taking into account bin-to-bin correlations in $\langle N \rangle$. These fits provided four values of $\alpha_s$ with statistical and systematic errors at each of the thirteen centre-of-mass energies. Taking into account the statistical and systematic correlations between the four measurements, they were combined into a single $\alpha_s$ result at each energy.

### 6.1 *n*-Jet Fractions

The $n$-jet fractions for the $Z^0$-calibration sample and those for the LEP1.5 and the two LEP2 samples are shown in Figures 3 to 7. Each plot shows the fraction of events in a given sample that were determined to be $n$-jets for a given value of jet resolution parameter at the hadron level. The jet fractions were calculated using five different clustering algorithms. For the Cone algorithm, both the $R$ and $\varepsilon$ variants are plotted, showing the individual $n$-jet fractions for $n \leq 2$, $n = 3$ and $n \geq 4$ in Figures 3 to 4. Similarly the $n$-jet fractions for the JADE algorithm are shown in Figure 5 for $n = 2, 3, 4, 5$. Figures 6 to 7 show the individual $n$-jet fractions for $n = 2, 3, 4, 5$ for the Durham and Cambridge algorithms respectively. The error bars on the points represent the total statistical and systematic errors added in quadrature. The Monte Carlo expectations corresponding to PYTHIA and HERWIG are also displayed on each plot, for each algorithm and energy. The Monte Carlo expectations match the measured $n$-jet fractions reasonably well.

The differential two- three- and four-jet rates, $D_n$, are plotted as a function of $y_{\rm cut}$ for the Durham and Cambridge algorithms for the 91 GeV, the LEP1.5 and the two LEP2 data samples in Figures 8 and 9 respectively. Similarly, the average jet rates are plotted as a function of $y_{\rm cut}$ for the Durham and Cambridge algorithms for the 91 GeV, the LEP1.5 and the two LEP2 data samples in Figures 10 and 11 respectively. The curves on all the plots represent the expected Monte Carlo distributions. There is good agreement between the data and the expectations from both PYTHIA and HERWIG.

### 6.2 Fits to Determine the Value of $\alpha_s$

#### 6.2.1 Differential Two-jet Rates

All of the predictions described in Appendix A that hold for $R_2$ can also be applied the $D_2$ distribution since this is defined to be the difference between two neighbouring $R_2$ values divided by the difference, $\Delta y_{\rm cut}$, in their respective $y_{\rm cut}$ values,

$$D_2(y_{\rm cut}) \;=\; \frac{R_2(y_{\rm cut}) - R_2(y_{\rm cut} - \Delta y_{\rm cut})}{\Delta y_{\rm cut}}. \qquad (7)$$

Predictions based on $D_2$ were preferred over those based on $R_2$, as the differential two-jet rates have smaller statistical bin-to-bin correlations.

The range over which the $D_2$ and $\langle N \rangle$ distributions were fitted was determined by splitting the 91 GeV (and 189 GeV) PYTHIA Monte Carlo samples into 100 statistically independent subsamples. A fit was performed on each distribution (see, for example, Figure 8) for a number of possible end-points of the fit range (requiring that the fit range be at least six

bins). A $\chi^2$ per degree of freedom was determined for each fit range. The $\chi^2$ values were averaged over the 100 subsamples. The fit range that produced the smallest average $\chi^2$ per degree of freedom was chosen to be the default fit range for the Z-calibration (and high energy) datasets. Where no clear $\chi^2$ minimum was found, the largest reasonable range was chosen. The size of the fit range was then adjusted to ensure the range did not extend into a region where the hadronization corrections are too large, in particular at smaller $y_{\rm cut}$ values. A further adjustment was made to exclude fit ranges where one of the endpoints produces a sizeable contribution to the overall $\chi^2$ value. The systematic error on the fitted value of $\alpha_{\rm s}$ was determined by performing a separate fit for each of the variations in Table 3 and adding the differences with respect to the default value in quadrature.

The fits of the $\ln R$ matching prediction to the $D_2$ distribution are shown in Figure 12 for the Cambridge algorithm and in Figure 13 for the Durham algorithm. The values of $\alpha_{\rm s}$ determined from the $\ln R$ fits for the four datasets, together with a complete breakdown of statistical and systematic uncertainties, are given in Tables 4 and 5 for the Cambridge and Durham algorithms respectively.

#### 6.2.2 Average Jet Rates

For the average jet rates, $\langle N \rangle$, the statistical errors were strongly correlated between points, since the same events were used to determine $\langle N \rangle$ at each value of $y_{\rm cut}$. The fit was performed using a correlated $\chi^2$ fit in which the covariance matrix was determined from the PYTHIA Monte Carlo sample divided into many detector level subsamples. Each subsample was then corrected to the hadron level using a second, statistically independent, PYTHIA sample. There were 1500 subsamples created for the $\rm Z^0$-calibration dataset and 1000 subsamples created for the high energy datasets. The number of subsamples was chosen so that the elements of the covariance matrix would be stable and free of fluctuations.

An example of the fit of the $\ln R$ matching prediction to the $\langle N \rangle$ distribution is seen in Figure 14 for the Cambridge algorithm and in Figure 15 for the Durham algorithm. The values of $\alpha_{\rm s}$ determined from the $\ln R$ fits for the four datasets, together with a complete breakdown of statistical and systematic uncertainties, are given in Tables 6 and 7 for the Cambridge and Durham algorithms respectively.

#### 6.2.3 Running of $\alpha_{\rm s}$

The four values of $\alpha_{\rm s}$ determined from the $D_2$ and $\langle N \rangle$ distributions were combined into a single value at each centre-of-mass energy. The large statistical correlations between the four values were handled in a manner very similar to that for the bin-to-bin correlations of the average jet rates. For each of the four distributions, 1000 Monte Carlo samples were used to determine the statistical correlations between the $\alpha_{\rm s}$ values. The correlation matrices determined for the four separate energy points are given in Table 8. Using the statistical error for the $\alpha_{\rm s}$ value from each observable, the statistical covariance matrix was then determined. The full covariance matrix also included contributions from experimental, hadronization and theoretical errors

$$V = V_{\rm stat} + V_{\rm expt} + V_{\rm hadr} + V_{\rm theo} \tag{8}$$

A weight was determined for each of the $\alpha_s$ values from the inverse of the covariance matrix, $w_i = \sum_j (V^{-1})_{ij} / \sum_{ij} (V^{-1})_{ij}$. The combined $\alpha_s$ value was then determined from the sum of the product of the weights with the associated $\alpha_s$ value. Only statistical and experimental systematic errors were allowed to contribute to the off diagonal elements of the covariance matrix $V$, to ensure undesireable features such as negative weights where avoided. Hadronization and theoretical systematics where added only to the diagonal elements of the covariance matrix.

The statistical errors on the combined $\alpha_s$ value were determined from the product of the weights with the individual covariance matrices [41],

$$\sigma^2_{\rm stat} = w^T V_{\rm stat} w \tag{9}$$

The systematic errors are determined by running the combination for each systematic variation separately using the weights determined from the statistical and experimental errors only. The difference between these systematic combinations and the central value is taken as the systematic contribution to the error on the central value. The values of $\alpha_s$ determined for each centre-of-mass energy are given in Table 9 along with the breakdown of the uncertainties, both statistical and systematic. A comparison of the combined $\alpha_s$ values in Table 9 with those determined from the individual $D_2$ and $\langle N \rangle$ distributions is seen in Figure 16. Taking the combined $\alpha_s$ values at each centre-of-mass energy as an input, the value of $\alpha_s$ can be run back to the $Z^0$ pole using an $\mathcal{O}(\alpha_s^3)$ prediction. These $\alpha_s(M_{Z^0})$ values are also shown in Table 9 and plotted against the world average value of $\alpha_s(M_{Z^0})$=0.1172$\pm$0.002 [42] in Fig 17. Using these values taking into account proper statistical and systematic correlations a weighted mean of $\alpha_s(M_{Z^0})$=0.1197 $\pm$ 0.0010(stat.)$\pm$0.0012(expt.)$\pm$0.0021(had.)$\pm$0.0033(theo.) is determined. The four combined $\alpha_s$ values are plotted in Figure 18 as a function of the centre-of-mass energy, compared $\mathcal{O}(\alpha_s^2)$ to the energy evolution of $\alpha_s$ based on the determined value of $\alpha_s(M_{Z^0})$.

## 7 Summary and Conclusion

Data from twelve LEP 1.5 and LEP 2 datasets, with centre-of-mass energies ranging from 130 GeV to 207 GeV, were combined into three higher statistics datasets. These datasets and one combining several $Z^0$-calibration runs at 91 GeV were used to determine the $n$-jet fractions, the differential $n$-jet rates and the average jet rates for each of the energies. The different jet multiplicity distributions were compared to both PYTHIA and HERWIG Monte Carlo expectations.

Hadron-level $n$-jet fractions were determined using four jet clustering algorithms, CONE, JADE, Durham and Cambridge. For the CONE algorithm, measurements of the fraction of events with $n \leq 2$, 3, $\geq$4 jets are presented as functions of $R$ and $\varepsilon$. In the case of JADE, Durham and Cambridge measurements of the 2-, 3-, 4-, and 5-jet fractions were presented as functions of the jet resolution parameter, $y_{\rm cut}$. In all cases there is generally good agreement between the measured jet fractions and the Monte Carlo expectations.

Hadron-level determinations of the differential $n$-jet and average jet rates were performed for the Durham and Cambridge algorithms. The differential two-jet rate, $D_2$, and the average jet rate, $\langle N \rangle$ were used to determine the value of $\alpha_s(\sqrt{s})$ for each of the four combined energy

points. The determinations were carried out by fitting the parton level data distributions to $\ln R$ matching predictions over an appropriate range of $y_{\rm cut}$, with $\alpha_{\rm s}(\sqrt{s})$ as the variable parameter. The running of $\alpha_{\rm s}(\sqrt{s})$ was demonstrated by taking the four values of $\alpha_{\rm s}$ as determined from the combined datasets as a function of their centre-of-mass energies.

Using the measured values of $\alpha_{\rm s}(\sqrt{s})$ a value of $\alpha_{\rm s}(M_{\rm Z^0})$ was determined for each of the four datasets. There is good agreement between these four values of $\alpha_{\rm s}(M_{\rm Z^0})$ and the world average value of 0.1172±0.002. A weighted mean taking account of correlations, determined a final value of the strong coupling constant at $\sqrt{s}$ $M_{\rm Z^0}$ of $\alpha_{\rm s}(M_{\rm Z^0})$=$0.1197 \pm 0.0042$, where the error contains contributions from statistical, experimental, hadronization and theoretical uncertainties. The error on the determined value is slightly larger than that for the previous OPAL publication [11] which also used resummed predictions for $D_2$ and average jet rate distributions. This publication also explored slightly different energy ranges, including 35 and 45 GeV, and LEP1 up to only 189 GeV. This value agrees well with previous determinations of $\alpha_{\rm s}$ summarized in [43].

# Appendix

## A Theoretical Predictions

All QCD observables, like event shapes or jet rates, depend on the value of the strong coupling, $\alpha_{\rm s}(Q)$, where $Q$ is the energy scale at which the interaction takes place. Generally, the calculation of these observables requires taking a perturbative expansion in powers of $\alpha_{\rm s}(Q)$. Calculations of the expansion, based on calculated values of the QCD matrix elements [44], have been made only to second order, $\mathcal{O}(\alpha_{\rm s}^2)$. A general QCD observable, $R$, can be expressed to $\mathcal{O}(\alpha_{\rm s}^2)$ as

$$R(y) = a(y) + b(y)\alpha_{\rm s} + c(y)\alpha_{\rm s}^2, \tag{10}$$

where $yy_{\rm cut}$ for $R_n$, $D_n$. The coefficients for the case where $R(y)$=$R_2(y_{\rm cut})$ are tabulated in [45].

The truncation of the perturbative expansion at second order is only meaningful if the omitted higher order terms are negligible. In general, for large energies ($\geq$ 1 GeV) the value of $\alpha_{\rm s}$∼0.1 implies that $\alpha_{\rm s}^n$ will quickly approach zero as $n$ increases. However, terms containing these higher order $\alpha_{\rm s}$ values can only truly be neglected when the value of $y_{\rm cut}$ is relatively large. This is because the coefficients of the higher order $\alpha_{\rm s}$ terms are dependent on the logarithm of $y_{\rm cut}$ (in particular on a series of powers in $\ln(y_{\rm cut})$). In the case where $y_{\rm cut}$ becomes small the coefficients of the higher order terms can become sufficiently large that they can no longer be considered negligible, and the $\mathcal{O}(\alpha_{\rm s}^2)$ prediction is inaccurate.

### A.1 Next-to-Leading Log Approximation

In regions of small $y_{\rm cut}$, the perturbative expansion can be resummed in terms of an effective expansion parameter, $\alpha_{\rm s}L^2$, where $L = \ln(1/y_{\rm cut})$. The NLLA prediction for $R_2$ can thus be written as [34]

$$R_2^{\rm NLLA}(y_{\rm cut}) = (1 + K_1\overline{\alpha}_{\rm s} + K_2\overline{\alpha}_{\rm s}^2)\exp\big[Lg_1(\alpha_{\rm s}L) + g_2(\alpha_{\rm s}L)\big] \tag{11}$$

where $\overline{\alpha}_{\rm s} = \alpha_{\rm s}/2\pi$. The first coefficient $K_1$ is known exactly from the $\mathcal{O}(\alpha_{\rm s})$ matrix elements and the second coefficient $K_2$ is known from an integration of the $\mathcal{O}(\alpha_{\rm s}^2)$ matrix elements [46]. An NLLA

prediction also exists for the average jet rate distribution, and is given as [47]

$$\langle N\rangle^{NLLA}(y_{\rm cut}) \;=\; 2 + h_1(L\alpha_{\rm s}) + h_2(L\alpha_{\rm s})/L \tag{12}$$

where $h_i(L\alpha_{\rm s})$ corresponds to the sum of an infinite series of terms in powers of $L\alpha_{\rm s}$.

### A.2 Matched Predictions

The NLLA and $\mathcal{O}(\alpha_{\rm s}^2)$ predictions each contain terms that are missing in the other. In particular, the NLLA predictions contains $\alpha_{\rm s}$ terms of order larger than two, whereas the $\mathcal{O}(\alpha_{\rm s}^2)$ prediction implicitly contains terms of $\mathcal{O}(\alpha_{\rm s})$ and $\mathcal{O}(\alpha_{\rm s}^2)$ that appear in subleading terms in the NLLA and are hence neglected. In order to produce a more robust prediction, the NLLA and $\mathcal{O}(\alpha_{\rm s}^2)$ predictions can be matched. The simplest matching scheme, $R$-matching [48], involves expanding the exponential in the NLLA prediction; any terms that overlap with the $\mathcal{O}(\alpha_{\rm s}^2)$ prediction are then subtracted. The full $\mathcal{O}(\alpha_{\rm s}^2)$ prediction is then added to the NLLA prediction, giving

$$\begin{aligned} R_2(y_{\rm cut}) = R_2^{\rm NLLA}(y_{\rm cut}) - (K_1 + G_{11}L + G_{12}L^2)\overline{\alpha}_{\rm s} - \big[K_2 + G_{22}L^2 + G_{23}L^3 \\ +(G_{11}L + G_{12}L^2)(K_1 + \tfrac{1}{2}(G_{11}L + G_{12}L^2)\big]\overline{\alpha}_{\rm s}^2 + R_2^{\mathcal{O}(\alpha_s^2)}(y_{\rm cut}). \end{aligned} \tag{13}$$

The predictions for the average jet rates can be handled in an equivalent manner. First any terms overlapping with the $\mathcal{O}(\alpha_{\rm s}^2)$ prediction are subtracted from Eqn 12. The remaining terms are then added to the complete $\mathcal{O}(\alpha_{\rm s}^2)$ prediction to give,

$$\begin{aligned} \langle N\rangle(y_{\rm cut}) \;=\; & \langle N\rangle^{\rm NLLA}(y_{\rm cut}) - (H_{12}L^2 + H_{11}L)\overline{\alpha}_{\rm s} - (H_{24}L^4 + H_{23}L^3)\overline{\alpha}_{\rm s}^2 \\ & +\mathcal{A}_N(y_{\rm cut})\overline{\alpha}_{\rm s} + \mathcal{B}_N(y_{\rm cut})\overline{\alpha}_{\rm s}^2. \end{aligned} \tag{14}$$

where $\mathcal{A}_N(y_{\rm cut})$ corresponds to the coefficient for the $\mathcal{O}(\alpha_{\rm s})$ term and $\mathcal{B}_N(y_{\rm cut})$ corresponds to the coefficient for the $\mathcal{O}(\alpha_{\rm s}^2)$ term in the full $\langle N\rangle$ $\mathcal{O}(\alpha_{\rm s}^2)$ prediction.

An alternative approach to the $R$-matching scheme is the $\ln R$-matching prediction [48]. Under this approach the logarithm of the $\mathcal{O}(\alpha_{\rm s}^2)$ prediction is expanded and added to the logarithm of the NLLA prediction. Terms of $\mathcal{O}(\alpha_{\rm s}^3)$, as well as all non-logarithmic terms, are omitted from the expansion of the NLLA prediction prediction before matching. The resulting prediction for the two-jet rates is

$$\begin{aligned} \ln R(y_{\rm cut}) \;=\; & Lg_1(\alpha_{\rm s}L) + g_2(\alpha_{\rm s}L) - (G_{11}L + G_{12}L^2)\overline{\alpha}_{\rm s} - (G_{22}L^2 + G_{23}L^3)\overline{\alpha}_{\rm s}^2 \\ & +\mathcal{A}(y_{\rm cut})\overline{\alpha}_{\rm s} + \big[\mathcal{B}(y_{\rm cut}) - \tfrac{1}{2}\mathcal{A}(y_{\rm cut})^2\big]\,\overline{\alpha}_{\rm s}^2 \end{aligned} \tag{15}$$

where $\mathcal{A}(y_{\rm cut})$ corresponds to the coefficient for the $\mathcal{O}(\alpha_{\rm s})$ term and $\mathcal{B}(y_{\rm cut})$ corresponds to the coefficient for the $\mathcal{O}(\alpha_{\rm s}^2)$ term in the full $R_2$ $\mathcal{O}(\alpha_{\rm s}^2)$ prediction. The ln$R$-matching prediction for the average jet rate distribution is given by

$$\begin{aligned} \ln[\langle N\rangle(y_{\rm cut}) - 1] \;=\; & \ln[\langle N\rangle^{\rm NLLA}(y_{\rm cut}) - 1] - (H_{11}L + H_{12}L^2)\overline{\alpha}_{\rm s} \\ & - \big[H_{24}L^4 + H_{23}L^3 + H_{22}L^2 - \tfrac{1}{2}(H_{11}L + H_{12}L^2)^2\big]\,\overline{\alpha}_{\rm s}^2 \\ & +\mathcal{A}_N(y_{\rm cut})\overline{\alpha}_{\rm s} + \big[\mathcal{B}_N(y_{\rm cut}) - \tfrac{1}{2}\mathcal{A}_N(y_{\rm cut})^2\big]\,\overline{\alpha}_{\rm s}^2 \end{aligned} \tag{16}$$

We used the ln$R$-matching prediction in fitting to the $D_2$ and $\langle N\rangle$ distributions as it is expected to give the most robust prediction, since subleading and non-logarithmic terms are expected to vanish whereas for $R$-matching they are simply ignored leading to less accurate results.

### A.3 Renormalization Scale Dependence

A dependence on the renormalization scale, $\mu$, is not expected in any full order prediction of jet rates or average jet multiplicities. However due to the omission of higher order terms, in particular in the $\mathcal{O}(\alpha_s^2)$ approximation, the perturbative prediction depends on the renormalization scale. There are fewer terms neglected in the NLLA, so its dependence on $\mu$ is not expected to be as large. In order to account for this dependence on the renormalization scale, several terms require modification, in particular [49],

$$\begin{aligned} \mathcal{B}(y_{\rm cut}) &\to \mathcal{B}(y_{\rm cut}) + \mathcal{A}(y_{\rm cut})\beta_0 \ln x_\mu \\ g_2(\alpha_{\rm s}L) &\to g_2(\alpha_{\rm s}L) + \beta_0\alpha_{\rm s}^2 \frac{dg_1(\alpha_{\rm s}L)}{d(\alpha_{\rm s}L)} \ln x_\mu \\ G_{22} &\to G_{22} + \beta_0 G_{12} \ln x_\mu \end{aligned} \tag{17}$$

where $x_\mu = \mu/Q$. In addition, $\alpha_{\rm s}$ must itself be modified:

$$\overline{\alpha}_{\rm s}(\mu) \to \overline{\alpha}_{\rm s}(Q) + \overline{\alpha}_{\rm s}^2(Q)\beta_0 \ln x_\mu \tag{18}$$

where $Q$ corresponds to the energy scale at which the interaction takes place. The matched predictions are expected to have smaller dependence on the renormalization scale, so they were fitted taking $x_\mu = 1.0$ as the default value. Dependence on the renormalization scale was investigateded as a systematic uncertainty through a variation of $x_\mu$ in the fits compared to that from the fit using the default value, as described above.

## References


[1] S. Menke, eConf **C010430**, M09 (2001).

[2] J. H. Kuhn and M. Steinhauser, Nucl. Phys. **B619**, 588 (2001).

[3] A. L. Kataev, G. Parente, and A. V. Sidorov, Nucl. Phys. **B573**, 405 (2000).

[4] J. Santiago and F. J. Yndurain, Nucl. Phys. **B563**, 45 (1999).

[5] J. H. Kim *et al.*, Phys. Rev. Lett. **81**, 3595 (1998).

[6] J. R. Ellis and M. Karliner, Phys. Lett. **B341**, 397 (1995).

[7] OPAL Collaboration, P. D. Acton *et al.*, Z. Phys. **C59**, 1 (1993).

[8] OPAL Collaboration, G. Alexander *et al.*, Z. Phys. **C72**, 191 (1996).

[9] OPAL Collaboration, K. Ackerstaff *et al.*, Z. Phys. **C75**, 193 (1997).

[10] OPAL Collaboration, G. Abbiendi *et al.*, Eur. Phys. J. **C16**, 185 (2000).

[11] JADE and OPAL Collaborations, P. Pfeifenschneider *et al.*, Eur. Phys. J. **C17**, 19 (2000).

[12] OPAL Collaboration, K. Ahmet *et al.*, Nucl. Instrum. Meth. **A305**, 275 (1991).

[13] OPAL Collaboration, G. Abbiendi *et al.*, Eur. Phys. J. **C14**, 373 (2000).

[14] OPAL Collaboration, M. Arignon *et al.*, Nucl. Instrum. Meth. **A313**, 103 (1992).

[15] OPAL Collaboration, J. T. M. Baines *et al.*, Nucl. Instrum. Meth. **A325**, 271 (1993).

[16] OPAL Collaboration, J. Allison *et al.*, Nucl. Instrum. Meth. **A317**, 47 (1992).

[17] T. Sjöstrand *et al.*, Comput. Phys. Commun. **135**, 238 (2001).

[18] T. Sjöstrand, Comput. Phys. Commun. **82**, 74 (1994).

[19] G. Corcella *et al.*, JHEP **01**, 010 (2001).

[20] OPAL Collaboration, G. Alexander *et al.*, Z. Phys. **C69**, 534 (1996).

[21] OPAL Collaboration, G. Abbiendi *et al.*, Tests of models of color reconnection and a search for glueballs using gluon jets with a rapidity gap, (2003), hep-ex/0306021, CERN-EP-2003-031, to be published in Eur.Phys.J. **C**.

[22] S. Jadach, B. Ward, and Z. Was, Comput. Phys. Commun. **130**, 260 (2000).

[23] M. Skrzypek, S. Jadach, W. Placzek, and Z. Was, Comput. Phys. Commun. **94**, 216 (1996).

[24] J. Fujimoto *et al.*, Comput. Phys. Commun. **100**, 128 (1997).

[25] LEP, A combination of preliminary electroweak measurements and constraints on the standard model, 2003, hep-ex/0312023.

[26] OPAL Collaboration, K. Ackerstaff *et al.*, Eur. Phys. J. **C2**, 441 (1998).

[27] OPAL Collaboration, G. Alexander *et al.*, Z. Phys. **C52**, 175 (1991).

[28] OPAL Collaboration, K. Ackerstaff *et al.*, Eur. Phys. J. **C2**, 213 (1998).

[29] OPAL Collaboration, G. Abbiendi *et al.*, Eur. Phys. J. **C12**, 567 (2000).

[30] S. Brandt, C. Peyrou, R. Sosnowski, and A. Wroblewski, Phys. Lett. **12**, 57 (1964).

[31] OPAL Collaboration, K. Ackerstaff *et al.*, Phys. Lett. **B391**, 221 (1997).

[32] OPAL Collaboration, G. Abbiendi *et al.*, Eur. Phys. J. **C16**, 185 (2000).

[33] OPAL, G. Abbiendi *et al.*, Phys. Lett. **B493**, 249 (2000).

[34] S. Catani, Y. Dokshitzer, M. Olsson, G. Turnock, and B. Webber, Phys. Lett. **B269**, 432 (1991).

[35] Y. L. Dokshitzer, G. D. Leder, S. Moretti, and B. R. Webber, JHEP **08**, 001 (1997).

[36] JADE Collaboration, W. Bartel *et al.*, Z. Phys. **C33**, 23 (1986).

[37] F. Abe *et al.*, Phys. Lett. **D45**, 1448 (1992).

[38] OPAL Collaboration, K. Ackerstaff *et al.*, Z. Phys. **C75**, 193 (1997).

[39] M. Dasgupta and G. P. Salam, JHEP **08**, 032 (2002).

[40] R. W. L. Jones, M. Ford, G. P. Salam, H. Stenzel, and D. Wicke, JHEP **12**, 007 (2003).

[41] L. Lyons, D. Gibaut, and P. Clifford, Nucl. Instrum. Meth. **A270**, 110 (1988).

[42] K. Hagiwara *et al.*, Physical Review D **66**, 1 (2002).

[43] S. Bethke, Nucl. Phys. Proc. Suppl. **121**, 74 (2003).

[44] R. K. Ellis, D. A. Ross, and A. E. Terrano, Nucl. Phys. **B178**, 421 (1981).

[45] Y. L. Dokshitzer, G. D. Leder, S. Moretti, and B. R. Webber, JHEP **08**, 001 (1997).

[46] G. Dissertori and M. Schmelling, Phys. Lett. **B361**, 167 (1995).

[47] S. Catani, Y. Dokshitzer, F. Fiorani, and B. Webber, Nucl. Phys. **B377**, 445 (1992).

[48] S. Catani, L. Trentadue, G. Turnock, and B. Webber, Nucl. Phys. **B407**, 3 (1992).

[49] OPAL Collaboration, P. Acton *et al.*, Z. Phys. **C59**, 1 (1993).

| Energy (GeV) | | Integrated | Number of Events | | | |
|---|---|---|---|---|---|---|
| MC Energy | Measured | Luminosity ($pb^{-1}$) | Data | JETSET/ PYTHIA | HERWIG | ARIADNE |
| 91 | 91.5 | 14.5 | 431349 | 459k | 443k | – |
| 130 | 130.1 | 5.3 | 1894 | 50k | 50k | – |
| 136 | 136.1 | 6.0 | 1800 | 50k | 50k | – |
| 161 | 161.3 | 10.1 | 1932 | 100k | 80k | – |
| 172 | 172.1 | 10.4 | 1824 | 100k | 80k | – |
| 183 | 182.7 | 57.7 | 8918 | 100k | 100k | 100k |
| 189 | 188.7 | 185.2 | 26936 | 500k | 100k | 100k |
| 192 | 191.6 | 29.5 | 4229 | 200k | 100k | 125k |
| 196 | 195.5 | 76.7 | 10706 | 200k | 100k | 100k |
| 200 | 199.5 | 79.3 | 10226 | 200k | 100k | 100k |
| 202 | 201.6 | 37.8 | 5009 | 200k | 100k | 100k |
| 205 | 204.8 | 82.0 | 10857 | 200k | 100k | 100k |
| 207 | 206.6 | 138.8 | 17576 | 375k | 100k | 100k |

Table 1: Integrated luminosity and the total number of events for all samples. Included in this table are the Monte Carlo samples used to correct and make comparisons with, the data. The measured energy represents a spread of energies around the quoted value. The 91 GeV dataset corresponds to the data collected during the $Z^0$-calibration runs.

| Dataset | | ISR Fit | Final |
|---|---|---|---|
| 91 GeV | Data | 395695 | 395695 |
| | MC Signal | 381383 ± 598 | 381383 ± 598 |
| 130 GeV | Data | 318 | 318 |
| | MC Signal | 368 ± 3 | 368 ± 3 |
| | non-rad eff(%) | 85.4 ± 1.4 | 85.4 ± 1.4 |
| | non-rad pur(%) | 72.9 ± 1.1 | 72.9 ± 1.1 |
| 136 GeV | Data | 312 | 312 |
| | MC Signal | 329 ± 3 | 329 ± 3 |
| | non-rad eff(%) | 85.5 ± 1.4 | 85.5 ± 1.4 |
| | non-rad pur(%) | 73.1 ± 1.1 | 73.1 ± 1.1 |
| 161 GeV | Data | 304 | 283 |
| | MC Signal | 281 ± 2 | 269 ± 2 |
| | 4f Bkgd | 18 ± 4 | 5 ± 2 |
| | non-rad eff(%) | 83.4 ± 1.0 | 80.0 ± 1.0 |
| | non-rad pur(%) | 76.4 ± 0.9 | 72.5 ± 0.9 |
| | purity (%) | 93.8 ± 1.7 | 97.9 ± 1.4 |
| 172 GeV | Data | 280 | 224 |
| | MC Signal | 232 ± 1 | 222 ± 1 |
| | 4f Bkgd | 56 ± 7 | 10 ± 3 |
| | non-rad eff(%) | 83.3 ± 1.0 | 79.6 ± 1.0 |
| | non-rad pur(%) | 77.5 ± 0.9 | 73.4 ± 0.9 |
| | bkgd purity (%) | 80.3 ± 2.2 | 95.6 ± 1.7 |
| 183 GeV | Data | 1456 | 1077 |
| | MC Signal | 1074 ± 8 | 1023 ± 8 |
| | 4f Bkgd | 404 ±20 | 60 ±7 |
| | non-rad eff(%) | 83.0 ± 1.0 | 79.0 ± 1.0 |
| | non-rad pur(%) | 78.4 ± 0.9 | 73.7 ± 0.9 |
| | bkgd purity (%) | 72.7 ± 1.2 | 94.5 ± 1.2 |
| 189 GeV | Data | 4448 | 3086 |
| | MC Signal | 3148 ± 10 | 2959 ±10 |
| | 4f Bkgd | 1349 ± 36 | 171 ± 13 |
| | non-rad eff(%) | 83.0 ± 0.4 | 78.1 ± 0.4 |
| | non-rad pur(%) | 78.6 ± 0.4 | 73.7 ± 0.4 |
| | bkgd purity (%) | 70.0 ± 0.6 | 94.5 ± 0.6 |

| Dataset | | ISR Fit | Final |
|---|---|---|---|
| 192 GeV | Data | 717 | 514 |
| | MC Signal | 478±2 | 447±2 |
| | 4f Bkgd | 218±14 | 24±4 |
| | non-rad eff(%) | 82.8±0.7 | 77.4±0.7 |
| | non-rad pur(%) | 78.7 ± 0.6 | 73.6 ± 0.6 |
| | bkgd purity (%) | 68.7±1.5 | 94.7±1.2 |
| 196 GeV | Data | 1732 | 1137 |
| | MC Signal | 1176±6 | 1095±5 |
| | 4f Bkgd | 570±23 | 67±8 |
| | non-rad eff(%) | 82.7±0.7 | 77.1±0.6 |
| | non-rad pur(%) | 78.4 ± 0.6 | 73.3 ± 0.6 |
| | bkgd purity (%) | 67.4±1.0 | 94.2±1.0 |
| 200 GeV | Data | 1636 | 1090 |
| | MC Signal | 1231 ±6 | 1147±6 |
| | 4f Bkgd | 622±24 | 73±8 |
| | non-rad eff(%) | 82.6±0.7 | 76.9±0.7 |
| | non-rad pur(%) | 78.1 ± 0.6 | 72.9 ± 0.6 |
| | bkgd purity (%) | 66.4±1.0 | 94.0±1.0 |
| 202 GeV | Data | 806 | 519 |
| | MC Signal | 530±2 | 495±2 |
| | 4f Bkgd | 274±16 | 32±5 |
| | non-rad eff(%) | 85.4±0.7 | 76.9±0.7 |
| | non-rad pur(%) | 78.2 ± 0.6 | 72.9 ± 0.6 |
| | bkgd purity (%) | 65.9±1.4 | 93.8±1.2 |
| 205 GeV | Data | 1687 | 1130 |
| | MC Signal | 1104±6 | 1022±5 |
| | 4f Bkgd | 589±24 | 67±8 |
| | non-rad eff(%) | 82.4±0.7 | 76.3±0.7 |
| | non-rad pur(%) | 78.5 ± 0.7 | 73.4 ± 0.6 |
| | bkgd purity (%) | 65.2±1.0 | 93.8±1.0 |
| 207 GeV | Data | 2713 | 1717 |
| | MC Signal | 1832±7 | 1693±7 |
| | 4f Bkgd | 975±31 | 111±10 |
| | non-rad eff(%) | 82.7±0.5 | 76.5±0.5 |
| | non-rad pur(%) | 78.6 ± 0.5 | 73.5 ± 0.5 |
| | bkgd purity (%) | 65.3±0.8 | 94.6±0.6 |

Table 2: Effect of selection cuts (see text) on the number of observed events and the expected $q\overline{q}$ signal and four-fermion backgrounds. Also shown is the expected efficiency for selecting non-radiative $q\overline{q}$ events as well as the purity of true non-radiative events (determined as those events with $\sqrt{s}$-$\sqrt{s}'_{\rm true}$ <1 GeV) within the selected sample. The purity of the selected $q\overline{q}$ samples with respect to the expected total background is also presented. There is no expected four fermion background for the 91, 130 and 136 GeV data samples, so background rejection cuts were not applied there.

| Category | Error Source | Standard | Variation 1 | Variation 2 |
|---|---|---|---|---|
| (exp.) | Tracking* | MT objects | Tracks + Clusters | |
| | Containment ($\lvert\cos\theta_{\mathrm{T}}\rvert$)* | $< 0.9$ | $< 0.7$ | – |
| | qqqq ($\mathcal{L}_{\mathrm{qqqq}}$) | $< 0.25$ | $< 0.1$ | $< 0.4$ |
| | qql$\nu$($\mathcal{L}_{\mathrm{qq}\ell\nu}$) | $< 0.5$ | $< 0.75$ | $< 0.25$ |
| | Backgrounds ($\sigma_{\mathrm{bkgd}}$) | 1.0 | +5% | -5% |
| | ISR Algorithm | Default [26] | Alternative [38] | – |
| | Detector Correction* | PYTHIA | HERWIG | |
| (had.) | Hadronization* | PYTHIA | HERWIG | – |
| (theo.) | Fit Range* | min 6 bins | +2(1) bins | -2 bins |
| | Renorm. Scale Dep. ($x_\mu$)* | 1 | 0.5 | 2.0 |

Table 3: Summary of systematic variations applied to the datasets. The $*$ indicates which of the systematic variations were used for the 91 GeV dataset.

| | 91 GeV | 133 GeV | 179 GeV | 198 GeV |
|---|---|---|---|---|
| $\alpha_s$ ($\sqrt{s}$) | 0.1160 | 0.1080 | 0.1003 | 0.1010 |
| Fit Range ($-\log y_{cut}$) | 1.93 – 0.81 | 2.75 – 0.75 | 2.75 – 0.50 | 2.75 – 0.50 |
| $\chi^2$ /dof | 11.36/9 | 6.99/8 | 16.23/9 | 9.34/9 |
| Experimental | $\pm 0.0021$ | $\pm 0.0030$ | $\pm 0.0028$ | $\pm 0.0007$ |
| Hadronization | $-0.0057$ | $-0.0012$ | $-0.0015$ | $-0.0008$ |
| Bin Range | $\pm 0.0005$ | $\pm 0.0043$ | $\pm 0.0012$ | $\pm 0.0005$ |
| $x_\mu$ | $^{-0.0031}_{+0.0010}$ | $^{-0.0032}_{+0.0014}$ | $^{-0.0023}_{+0.0013}$ | $^{-0.0026}_{+0.0012}$ |
| $x_L$ | $^{-0.0041}_{+0.0025}$ | $^{-0.0034}_{+0.0020}$ | $^{-0.0026}_{+0.0019}$ | $^{-0.0027}_{+0.0017}$ |
| Theoretical | $\pm 0.0032$ | $\pm 0.0054$ | $\pm 0.0026$ | $\pm 0.0026$ |
| Total Stat. | $\pm 0.0004$ | $\pm 0.0038$ | $\pm 0.0028$ | $\pm 0.0012$ |
| Total Syst. | $\pm 0.0068$ | $\pm 0.0063$ | $\pm 0.0041$ | $\pm 0.0028$ |
| Total Error | $\pm 0.0068$ | $\pm 0.0073$ | $\pm 0.0049$ | $\pm 0.0030$ |

Table 4: Determination of $\alpha_s$ and the breakdown of statistical and systematic errors from the fit to the Cambridge differential two-jet rate distribution ($D_2^C$) for all centre-of-mass energy values. The quality of the fit is characterized by the chi-square ($\chi^2$) and the number of degrees of freedom (dof). The theoretical error includes contributions from the bin range and $x_\mu$ variations and excludes the $x_L$ variation.

| | 91 GeV | 133 GeV | 179 GeV | 198 GeV |
|---|---|---|---|---|
| $\alpha_s$ ($\sqrt{s}$) | 0.1209 | 0.1118 | 0.1068 | 0.1074 |
| Fit Range ($-\log y_{cut}$) | 1.81 – 0.81 | 2.75 – 0.75 | 2.75 – 0.50 | 2.50 – 0.75 |
| $\chi^2$/dof | 15.99/10 | 7.76/8 | 6.71/9 | 12.08/9 |
| Experimental | $\pm 0.0026$ | $\pm 0.0046$ | $\pm 0.0023$ | $\pm 0.0008$ |
| Hadronization | $-0.0048$ | $-0.0025$ | $-0.0015$ | $-0.0009$ |
| Bin Range | $\pm 0.0004$ | $\pm 0.0030$ | $\pm 0.0015$ | $\pm 0.0007$ |
| $x_\mu$ | $^{-0.0038}_{+0.0015}$ | $^{-0.0036}_{+0.0014}$ | $^{-0.0032}_{+0.0019}$ | $^{-0.0031}_{+0.0014}$ |
| $x_L$ | $^{-0.0045}_{+0.0028}$ | $^{-0.0037}_{+0.0021}$ | $^{-0.0030}_{+0.0021}$ | $^{-0.0031}_{+0.0019}$ |
| Theoretical | $\pm 0.0038$ | $\pm 0.0047$ | $\pm 0.0035$ | $\pm 0.0032$ |
| Total Stat. | $\pm 0.0004$ | $\pm 0.0046$ | $\pm 0.0034$ | $\pm 0.0014$ |
| Total Syst. | $\pm 0.0066$ | $\pm 0.0070$ | $\pm 0.0044$ | $\pm 0.0034$ |
| Total Error | $\pm 0.0066$ | $\pm 0.0084$ | $\pm 0.0056$ | $\pm 0.0036$ |

Table 5: Determination of $\alpha_s$ and the breakdown of statistical and systematic errors from the fit to the Durham differential two-jet rate distribution ($D_2^D$) for all centre-of-mass energy values. The quality of the fit is characterized by the chi-square ($\chi^2$) and the number of degrees of freedom (dof). The theoretical error includes contributions from the bin range and $x_\mu$ variations and excludes the $x_L$ variation.

| | 91 GeV | 133 GeV | 179 GeV | 198 GeV |
|---|---|---|---|---|
| $\alpha_s$ ($\sqrt{s}$) | 0.1241 | 0.1168 | 0.1069 | 0.1070 |
| Fit Range ($-\log y_{cut}$) | 2.31 – 0.68 | 2.75 – 0.50 | 2.75 – 0.50 | 2.75 – 0.50 |
| $\chi^2$/dof | 16.36/13 | 8.39/9 | 0.82/9 | 1.43/9 |
| Experimental | $\pm$0.0013 | $\pm$0.0041 | $\pm$0.0032 | $\pm$0.0011 |
| Hadronization | $-$0.0049 | $-$0.0006 | $-$0.0020 | $-$0.0010 |
| Bin Range | $\pm$0.0007 | $\pm$0.0037 | $\pm$0.0022 | $\pm$0.0009 |
| $x_\mu$ | 0.0026 | 0.0021 | 0.0016 | 0.0017 |
| Theoretical | $\pm$0.0026 | $\pm$0.0043 | $\pm$0.0028 | $\pm$0.0019 |
| Total Stat. | $\pm$0.0005 | $\pm$0.0031 | $\pm$0.0038 | $\pm$0.0016 |
| Total Syst. | $\pm$0.0057 | $\pm$0.0059 | $\pm$0.0046 | $\pm$0.0023 |
| Total Error | $\pm$0.0057 | $\pm$0.0067 | $\pm$0.0060 | $\pm$0.0028 |

Table 6: Determination of $\alpha_s$ and the breakdown of statistical and systematic errors from the fit to the Cambridge average jet rate distribution ($\langle N \rangle^C$) for all centre-of-mass energy values. The quality of the fit is characterized by the chi-square ($\chi^2$) and the number of degrees of freedom (dof).

| | 91 GeV | 133 GeV | 179 GeV | 198 GeV |
|---|---|---|---|---|
| $\alpha_s$ ($\sqrt{s}$) | 0.1272 | 0.1191 | 0.1107 | 0.1112 |
| Fit Range ($-\log y_{cut}$) | 2.56 – 0.56 | 2.75 – 0.50 | 2.75 – 0.50 | 2.75 – 0.50 |
| $\chi^2$/dof | 15.55/16 | 6.16/9 | 0.13/9 | 1.08/9 |
| Experimental | $\pm$0.0006 | $\pm$0.0039 | $\pm$0.0028 | $\pm$0.0011 |
| Hadronization | $-$0.0044 | $-$0.0002 | $-$0.0009 | $-$0.0003 |
| Bin Range | $\pm$0.0006 | $\pm$0.0028 | $\pm$0.0001 | $\pm$0.0008 |
| $x_\mu$ | 0.0034 | 0.0028 | 0.0023 | 0.0023 |
| Theoretical | $\pm$0.0035 | $\pm$0.0040 | $\pm$0.0023 | $\pm$0.0025 |
| Total Stat. | $\pm$0.0003 | $\pm$0.0028 | $\pm$0.0033 | $\pm$0.0014 |
| Total Syst. | $\pm$0.0057 | $\pm$0.0056 | $\pm$0.0037 | $\pm$0.0026 |
| Total Error | $\pm$0.0057 | $\pm$0.0062 | $\pm$0.0050 | $\pm$0.0029 |

Table 7: Determination of $\alpha_s$ and the breakdown of statistical and systematic errors from the fit to the Durham average jet rate distribution ($\langle N \rangle^D$) for all centre-of-mass energy values. The quality of the fit is characterized by the chi-square ($\chi^2$) and the number of degrees of freedom (dof).

| 91 GeV | $D_2^C$ | $D_2^D$ | $\langle N \rangle^C$ | $\langle N \rangle^D$ |
|---|---|---|---|---|
| $D_2^C$ | 100.0 | 86.2 | 53.2 | 46.5 |
| $D_2^D$ | 86.2 | 100.0 | 56.0 | 47.8 |
| $\langle N \rangle^C$ | 53.2 | 56.0 | 100.0 | 75.8 |
| $\langle N \rangle^D$ | 46.5 | 47.8 | 75.8 | 100.0 |

| 133 GeV | $D_2^C$ | $D_2^D$ | $\langle N \rangle^C$ | $\langle N \rangle^D$ |
|---|---|---|---|---|
| $D_2^C$ | 100.0 | 93.1 | 67.9 | 59.2 |
| $D_2^D$ | 93.1 | 100.0 | 62.2 | 60.5 |
| $\langle N \rangle^C$ | 67.9 | 62.2 | 100.0 | 81.4 |
| $\langle N \rangle^D$ | 59.2 | 60.5 | 81.4 | 100.0 |

| 179 GeV | $D_2^C$ | $D_2^D$ | $\langle N \rangle^C$ | $\langle N \rangle^D$ |
|---|---|---|---|---|
| $D_2^C$ | 100.0 | 91.6 | 67.9 | 60.7 |
| $D_2^D$ | 91.6 | 100.0 | 66.4 | 65.4 |
| $\langle N \rangle^C$ | 67.9 | 66.4 | 100.0 | 82.4 |
| $\langle N \rangle^D$ | 60.7 | 65.4 | 82.4 | 100.0 |

| 198 GeV | $D_2^C$ | $D_2^D$ | $\langle N \rangle^C$ | $\langle N \rangle^D$ |
|---|---|---|---|---|
| $D_2^C$ | 100.0 | 92.2 | 73.4 | 65.2 |
| $D_2^D$ | 92.2 | 100.0 | 69.9 | 70.5 |
| $\langle N \rangle^C$ | 73.4 | 69.9 | 100.0 | 82.4 |
| $\langle N \rangle^D$ | 65.2 | 70.5 | 82.4 | 100.0 |

Table 8: Correlation matrix determined for the combination of $\alpha_s$ measurements from the four different observables for each of the four different datasets. Each matrix element is presented as a percentage (%).

| | Value for $\sqrt{s}$ | | | | | Value at $M_{Z^0}$ | | | | |
|---|---|---|---|---|---|---|---|---|---|---|
| $\sqrt{s}$ (GeV) | $\alpha_s$ | $\sigma_{stat.}$ | $\sigma_{exp.}$ | $\sigma_{hadr.}$ | $\sigma_{theory}$ | $\alpha_s$ | $\sigma_{stat.}$ | $\sigma_{exp.}$ | $\sigma_{hadr.}$ | $\sigma_{theory}$ |
| $M_{Z^0}$ | 0.1227 | 0.0003 | 0.0012 | 0.0049 | 0.0032 | 0.1227 | 0.0003 | 0.0012 | 0.0049 | 0.0032 |
| 133 | 0.1150 | 0.0029 | 0.0035 | 0.0009 | 0.0045 | 0.1217 | 0.0033 | 0.0040 | 0.0010 | 0.0050 |
| 179 | 0.1060 | 0.0029 | 0.0026 | 0.0015 | 0.0027 | 0.1163 | 0.0035 | 0.0032 | 0.0018 | 0.0033 |
| 198 | 0.1062 | 0.0013 | 0.0008 | 0.0006 | 0.0025 | 0.1184 | 0.0016 | 0.0011 | 0.0008 | 0.0032 |

Table 9: Values of $\alpha_s$ determined from the statistically weighted average of the individual $\alpha_s$ results at each centre-of-mass energy, along with statistical and systematic errors. The value $\alpha_s$ for the dataset when run back to the $Z^0$ pole are given on the right half of the table with full statistical and systematic errors.

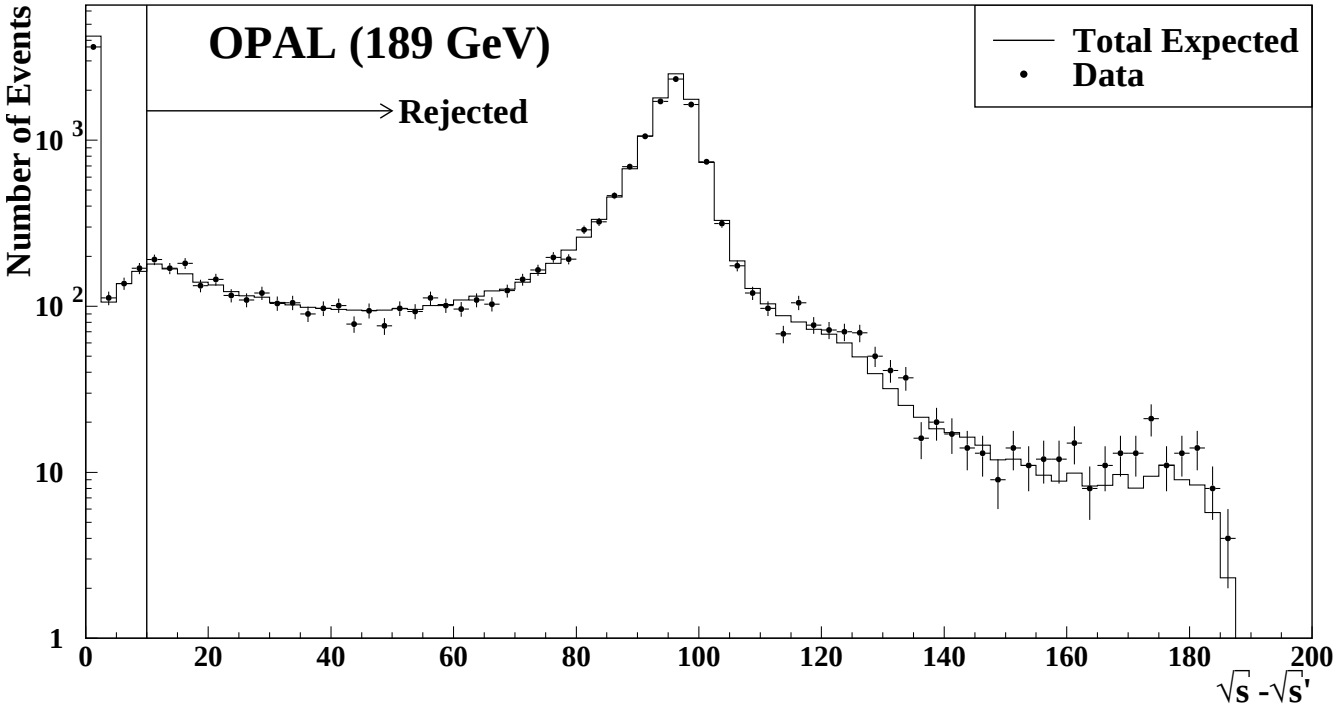


Figure 1: The $\sqrt{s} - \sqrt{s'}$ distribution for the 189 GeV dataset. The vertical line indicates where the cut was applied. The expected $q\overline{q}$ signal was determined from Monte Carlo and normalized to the luminosity of the measured sample. Vertical error bars indicate the size of statistical errors, while horizontal error bars correspond to the bin width.

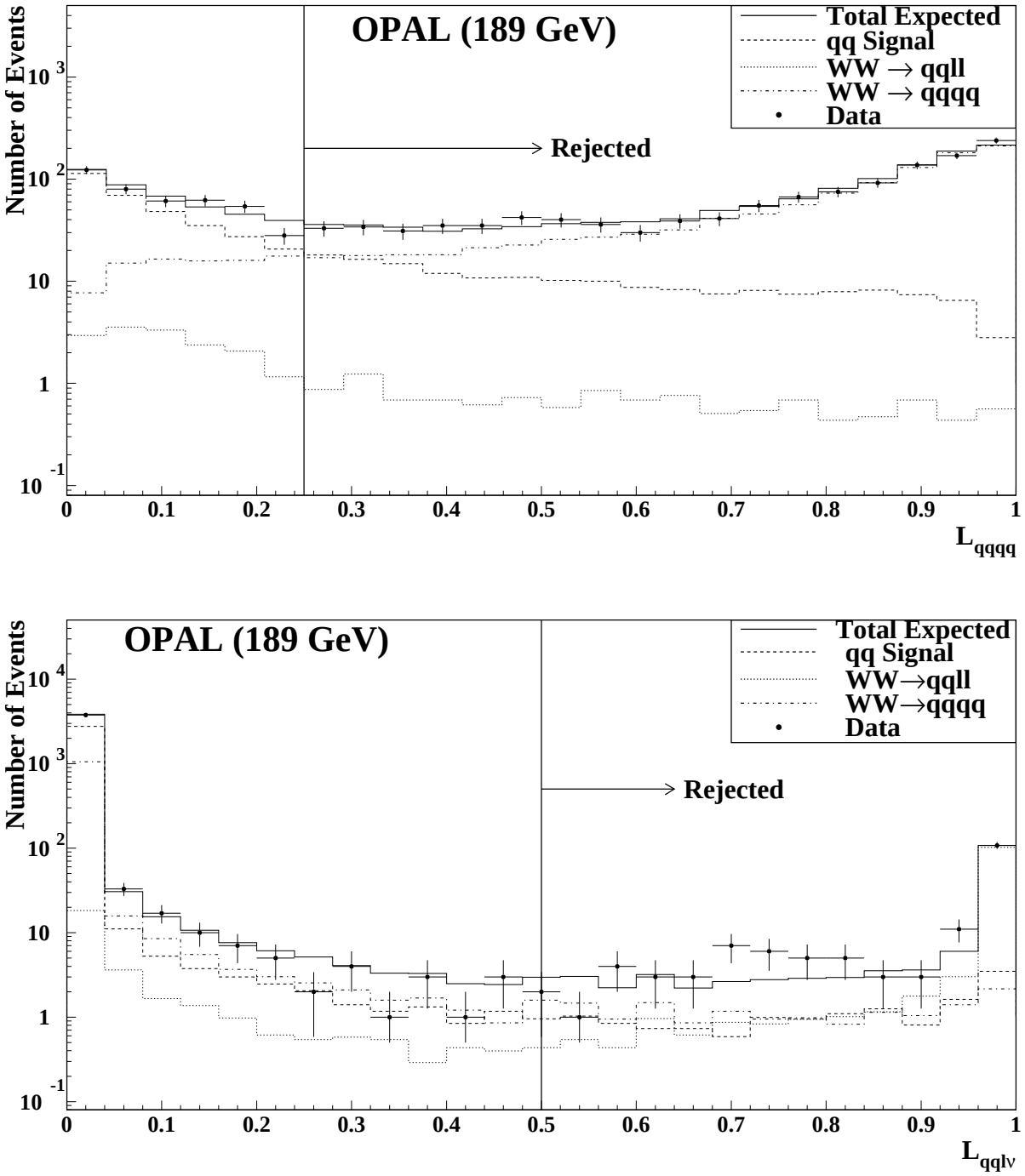


Figure 2: Distributions of the four-quark likelihood $\mathcal{L}_{\mathrm{qqqq}}$ (top) and semi-leptonic likelihood $\mathcal{L}_{\mathrm{qq}\ell\nu}$ (bottom) for the 189 GeV dataset. The expected contribution of the four-quark non-QCD background to the total sample is shown by the dotted line, and the expected $\mathrm{q\bar{q}}\ell\nu$ non-QCD backgrounds are represented by the dashed line. The vertical lines indicate the values of the parameters where the cuts were applied. The expected $\mathrm{q\overline{q}}$ signal was determined from Monte Carlo and normalized to the luminosity of the measured sample. Vertical error bars indicate the size of statistical errors, while the horizontal bars correspond to the binwidth.

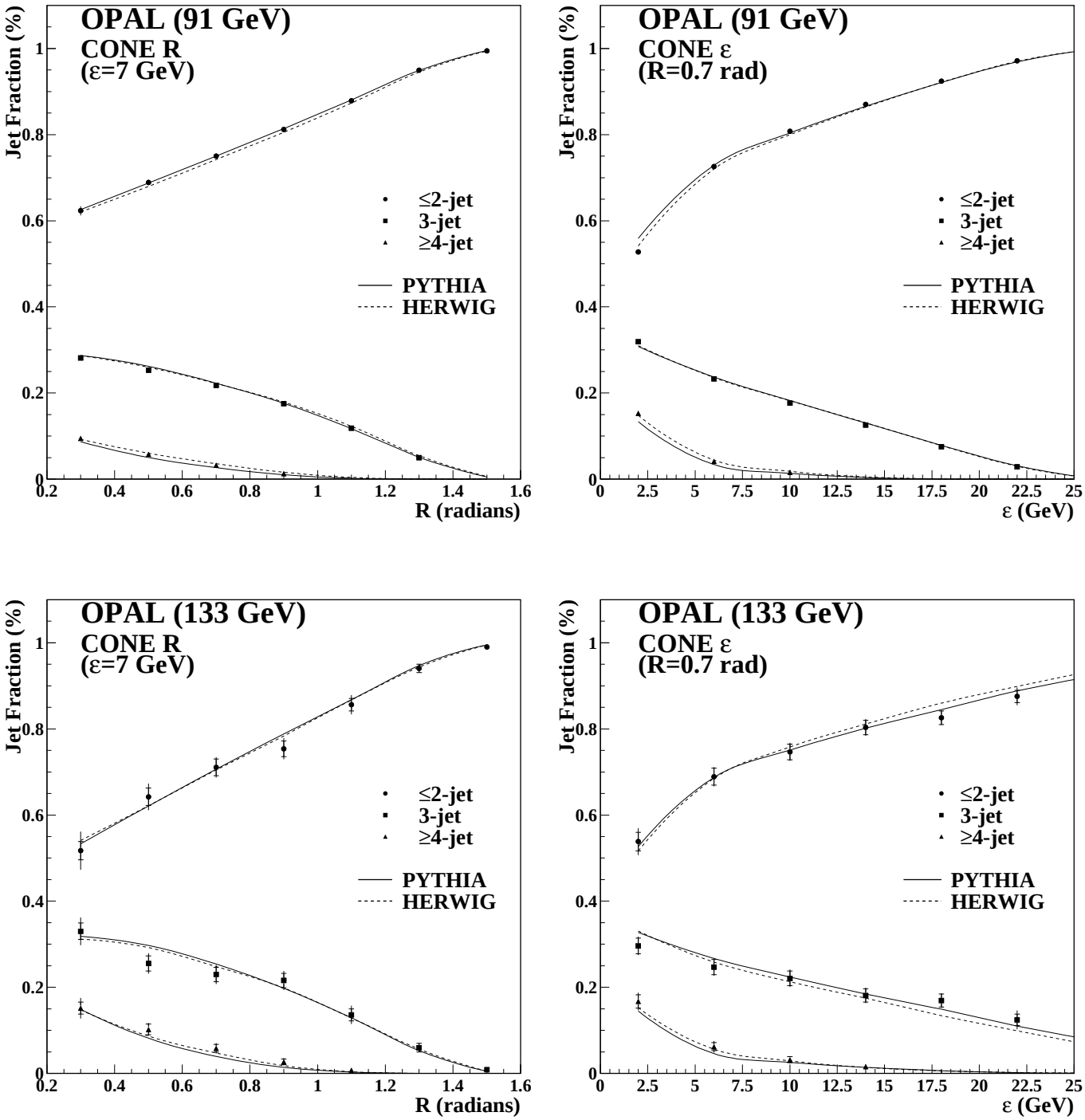


Figure 3: The hadron level $n$-jet rates for the $R$ and $\varepsilon$ variants of the CONE algorithm for the data with $\sqrt{s}$ = 91 GeV (top) and $\sqrt{s}$ = 133 GeV (bottom). In all plots the JETSET/PYTHIA and HERWIG Monte Carlo expectations are represented by the curves. Outer error bars indicate total errors while the inner bars indicate statistical errors.

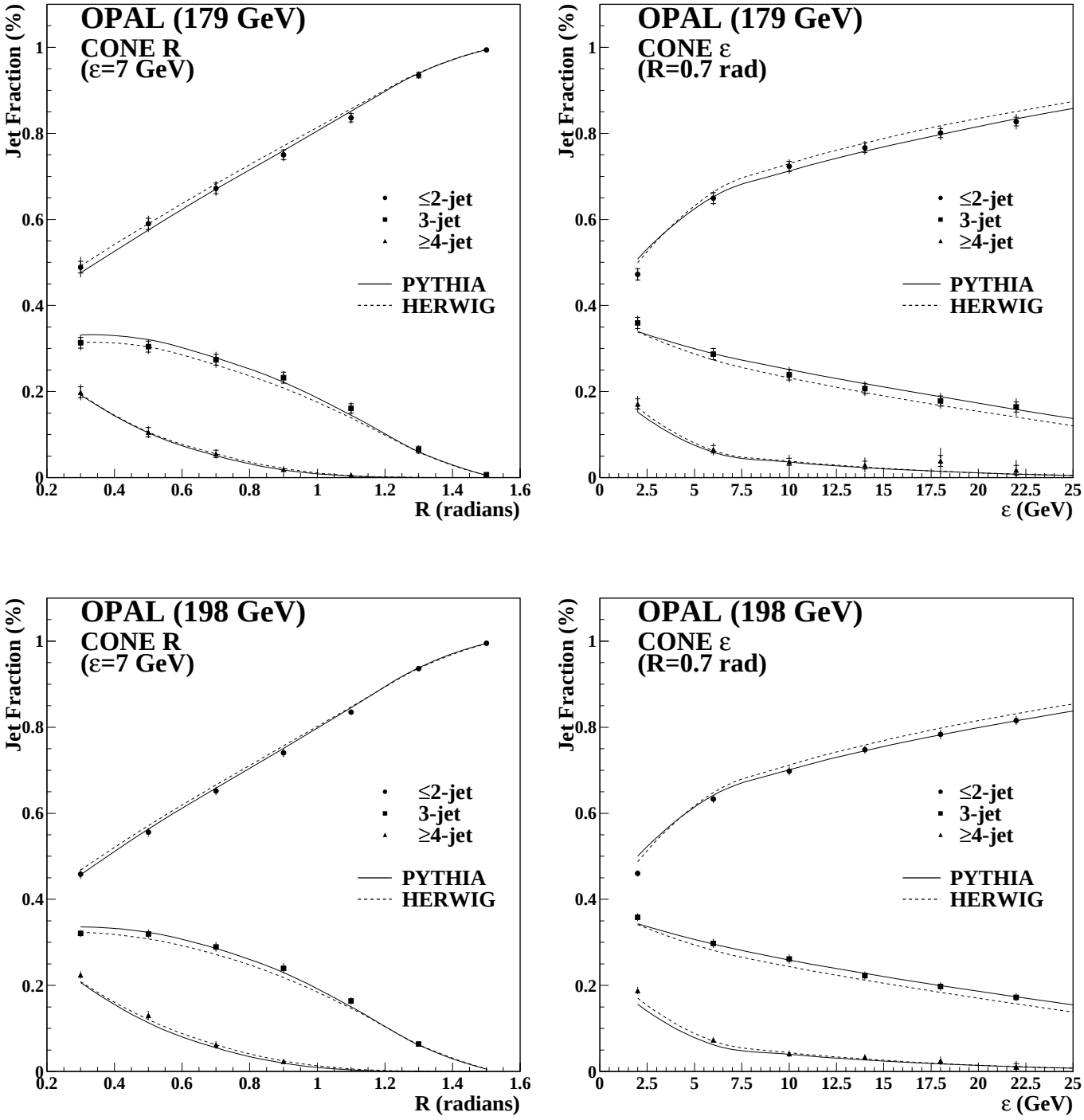


Figure 4: The hadron level $n$-jet rates for the $R$ and $\varepsilon$ variants of the CONE algorithm for the data with $\sqrt{s} = 179$ GeV (top) and $\sqrt{s} = 198$ GeV (bottom). In all plots the PYTHIA and HERWIG Monte Carlo expectations are represented by the curves. Outer error bars indicate total errors while the inner bars indicate statistical errors.

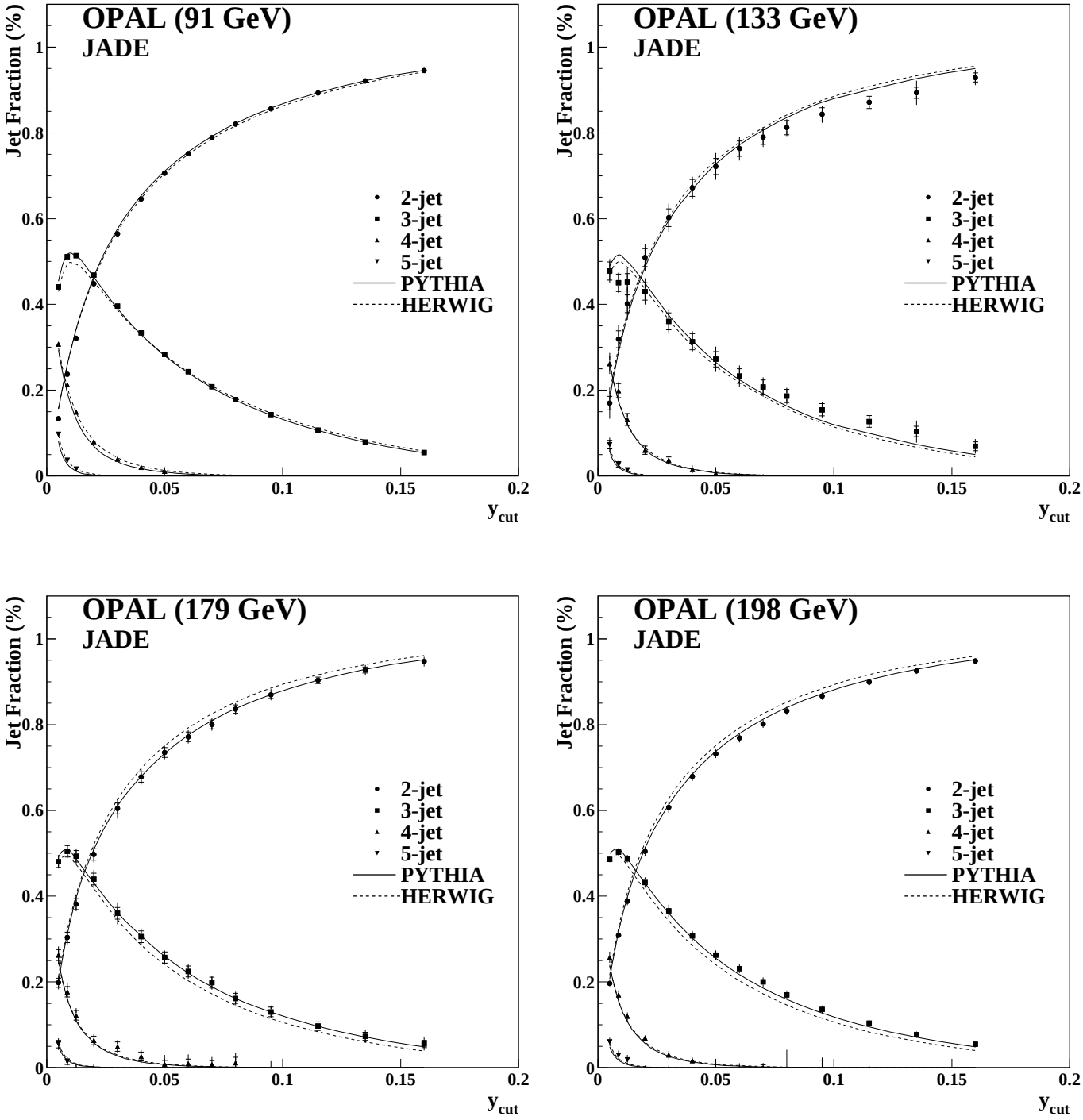


Figure 5: The hadron level $n$-jet rates for the JADE algorithm for the data with $\sqrt{s} = 91$ GeV (top left), $\sqrt{s} = 133$ GeV (top right), $\sqrt{s} = 179$ GeV (bottom left) and $\sqrt{s} = 198$ GeV (bottom right). In all plots the JETSET/PYTHIA and HERWIG Monte Carlo expectations are represented by the curves. Outer error bars indicate total errors while the inner bars indicate statistical errors.

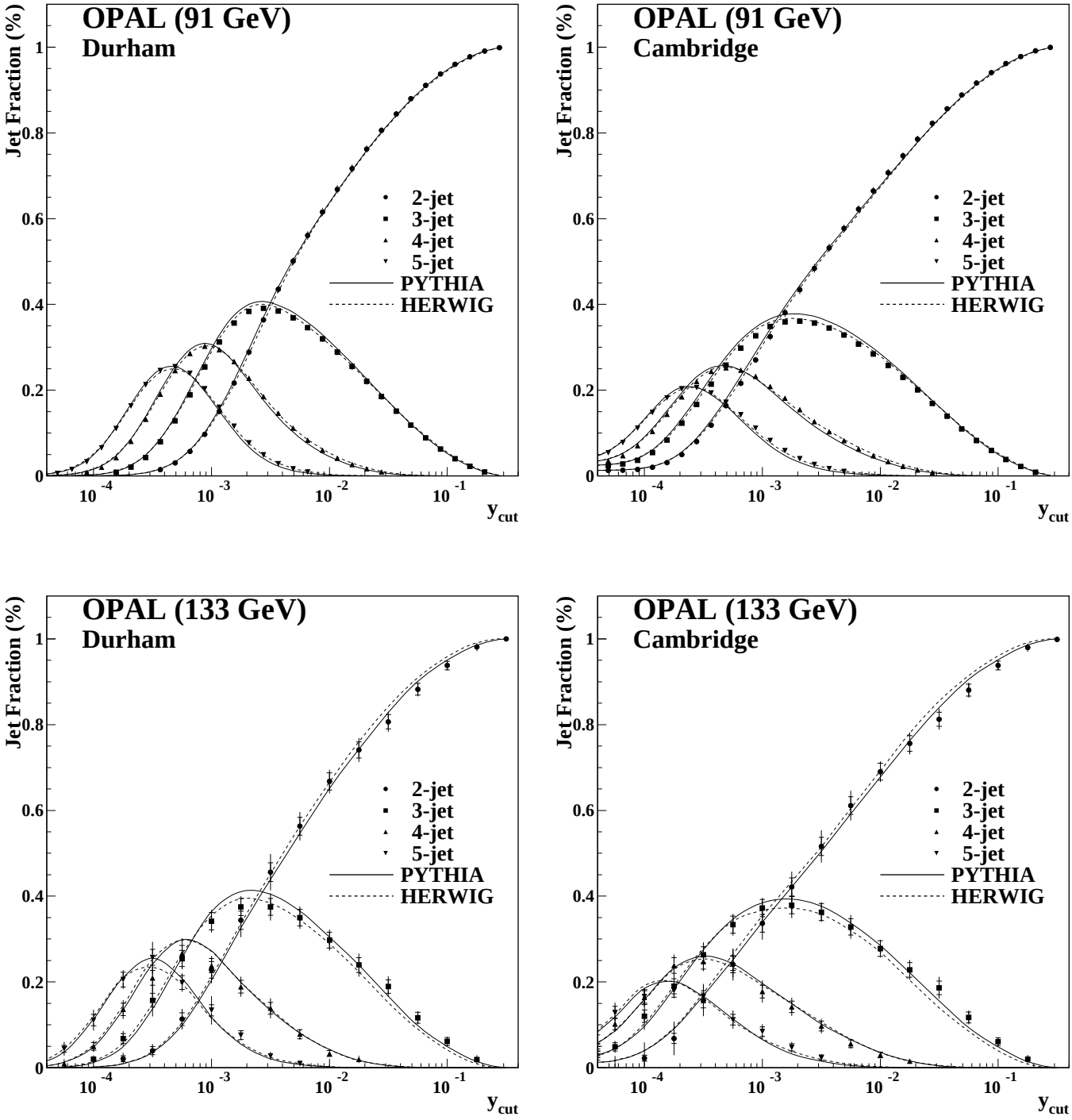


Figure 6: The hadron level $n$-jet rates for the Durham and Cambridge algorithms for the data with $\sqrt{s} = 91$ GeV (top) and $\sqrt{s} = 133$ GeV (bottom). In all plots the JETSET/PYTHIA and HERWIG Monte Carlo expectations are represented by the curves. Outer error bars indicate total errors while the inner bars indicate statistical errors.

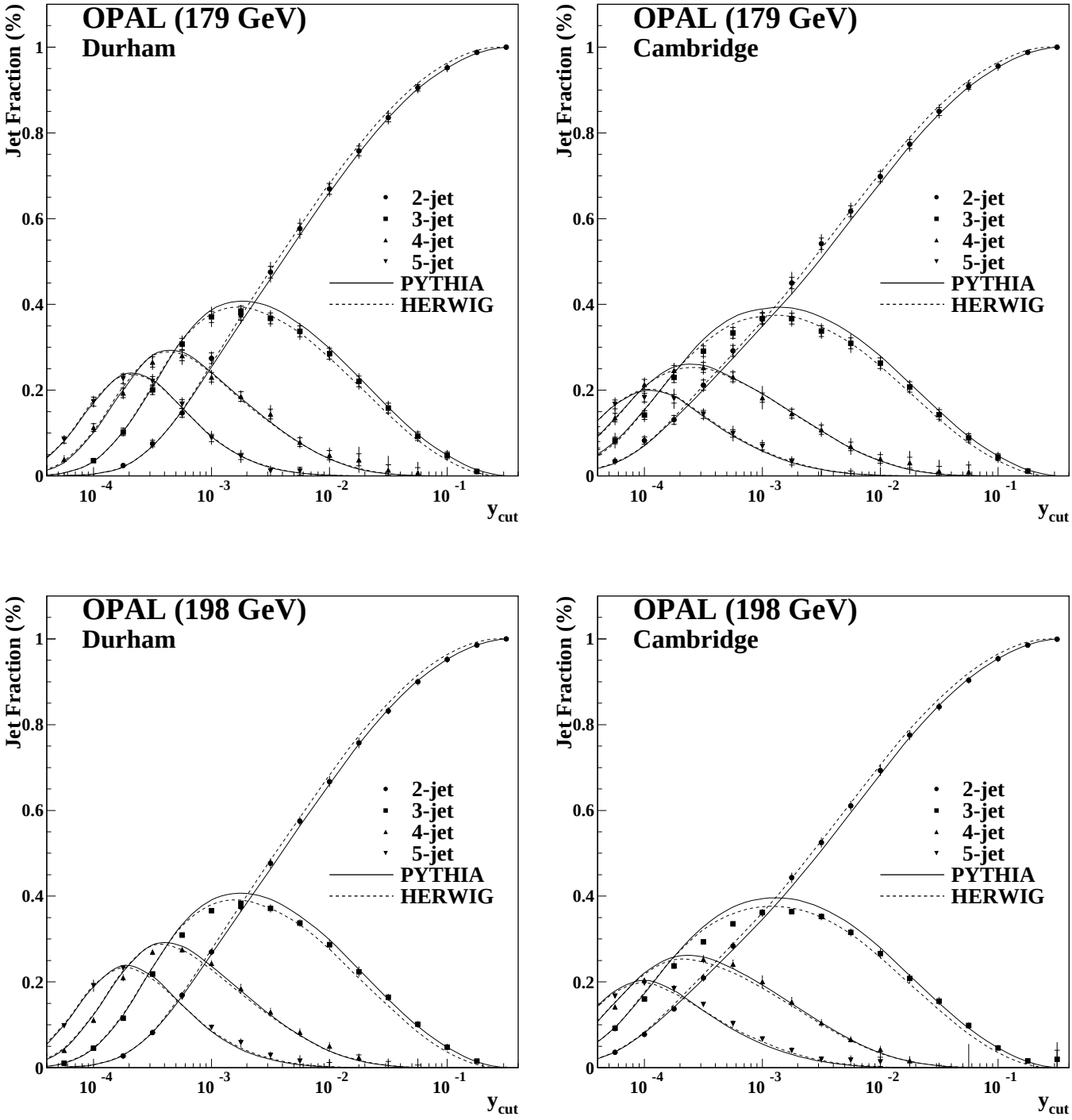


Figure 7: The hadron level $n$-jet rates for the Durham and Cambridge algorithms for the data with $\sqrt{s} = 179$ GeV (top) and $\sqrt{s} = 198$ GeV (bottom). In all plots the PYTHIA and HERWIG Monte Carlo expectations are represented by the curves. Outer error bars indicate total errors while the inner bars indicate statistical errors.

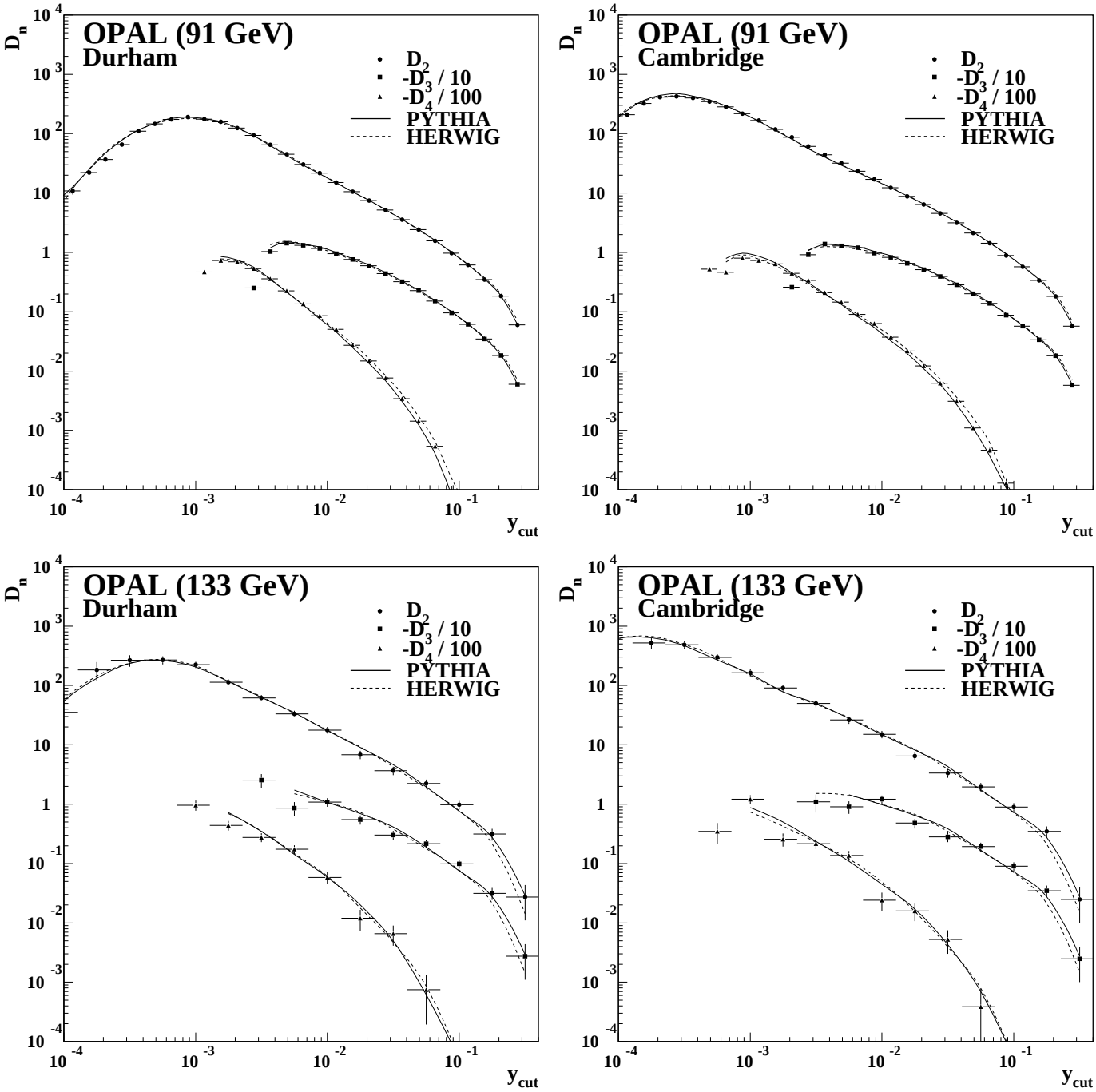


Figure 8: The differential 2-, 3- and 4-jet rates at the hadron level as a function of $y_{cut}$ for the Cambridge and Durham algorithms for data with $\sqrt{s} = 91$ GeV (top) and for the LEP1.5 combined dataset at $\sqrt{s} = 133$ GeV (bottom). PYTHIA and HERWIG Monte Carlo expectations are represented by the curves. The differential 3- and 4-jet rates have a negative slope in the region of large $y_{\rm cut}$ and therefore the negative values of $D_3$ and $D_4$ are plotted. Note that $D_3$ and $D_4$ are scaled down by one and two orders of magnitude, respectively, for clarity. Error bars indicate total (statistical + systematic) errors.

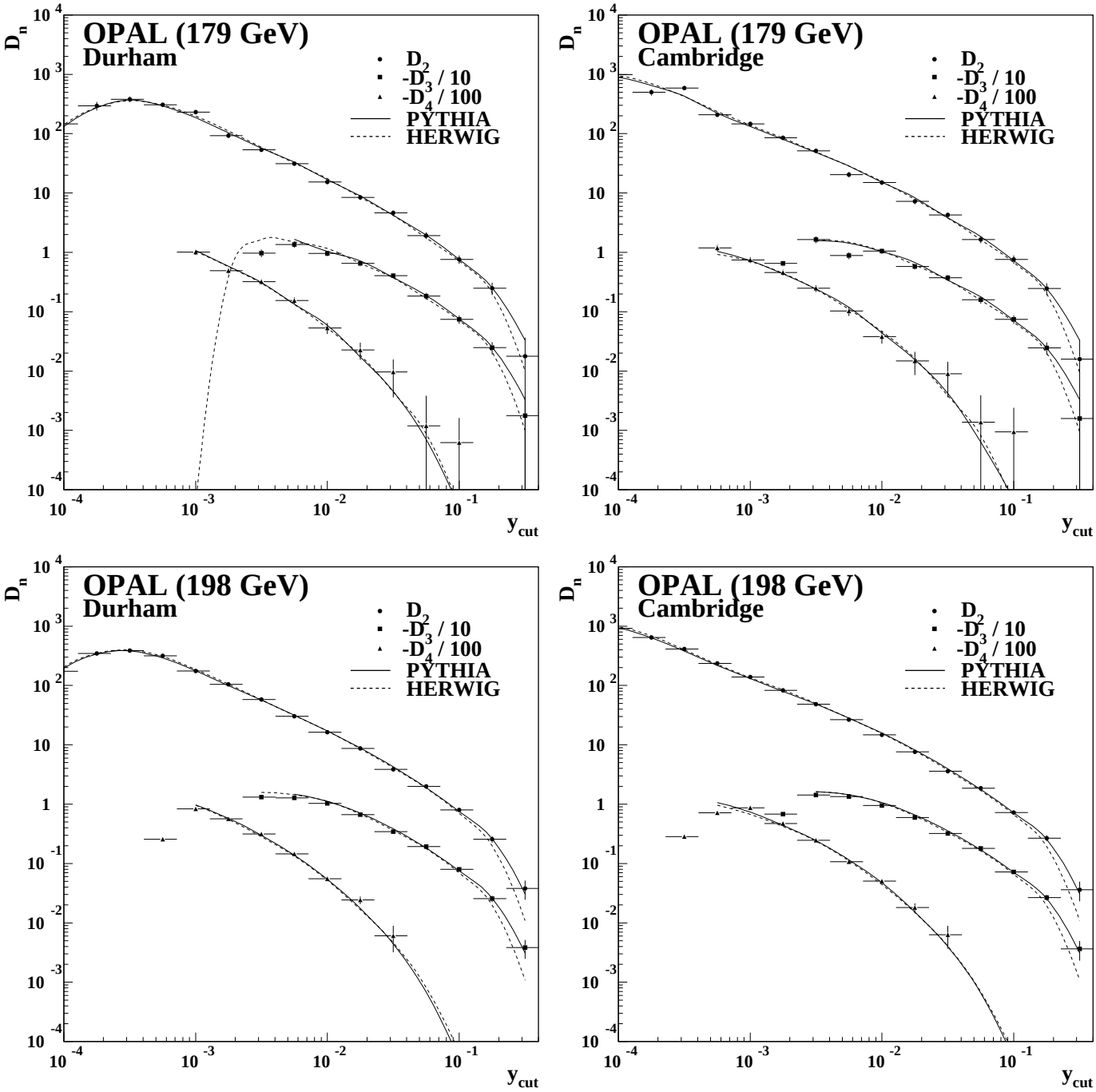


Figure 9: The differential 2-, 3- and 4-jet rates at the hadron level as a function of $y_{cut}$ for the Cambridge and Durham algorithms for two combined LEP2 datasets with $\sqrt{s} = 179$ GeV (top) and $\sqrt{s} = 198$ GeV (bottom). PYTHIA and HERWIG Monte Carlo expectations are represented by the curves. The differential 3- and 4-jet rates have a negative slope in the region of large $y_{\rm cut}$ and therefore the negative values of $D_3$ and $D_4$ are plotted. Note that $D_3$ and $D_4$ are scaled down by one and two orders of magnitude, respectively, for clarity. Error bars indicate total (statistical + systematic) errors.

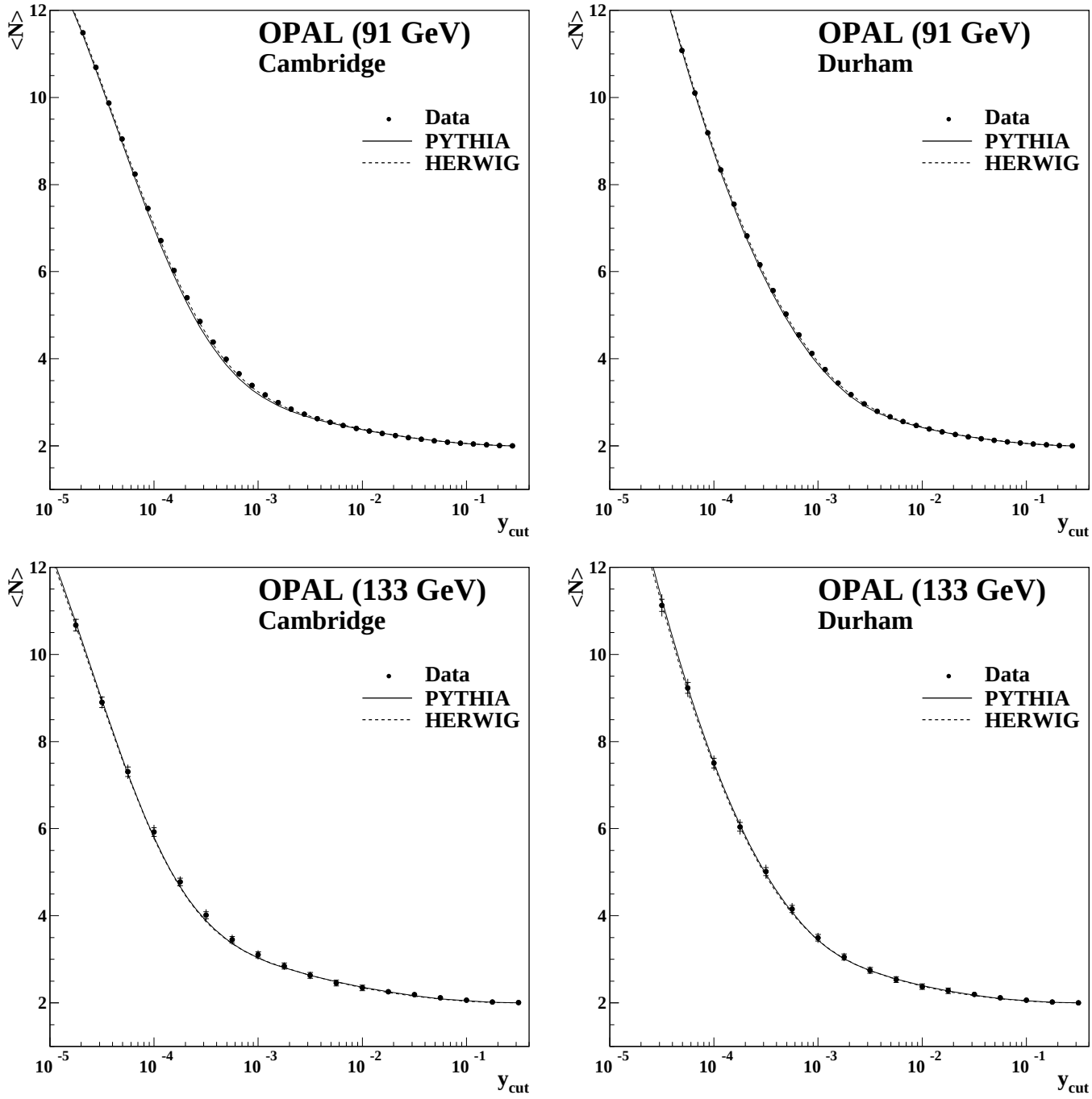


Figure 10: The average jet rates at the hadron level as a function of $y_{cut}$ for the Cambridge and Durham algorithms for the data with $\sqrt{s} = 91$ GeV (top) and for the LEP1.5 combined dataset at $\sqrt{s} = 133$ GeV(bottom). PYTHIA and HERWIG Monte Carlo expectations are represented by the curves. Error bars indicate total (statistical + systematic) errors.

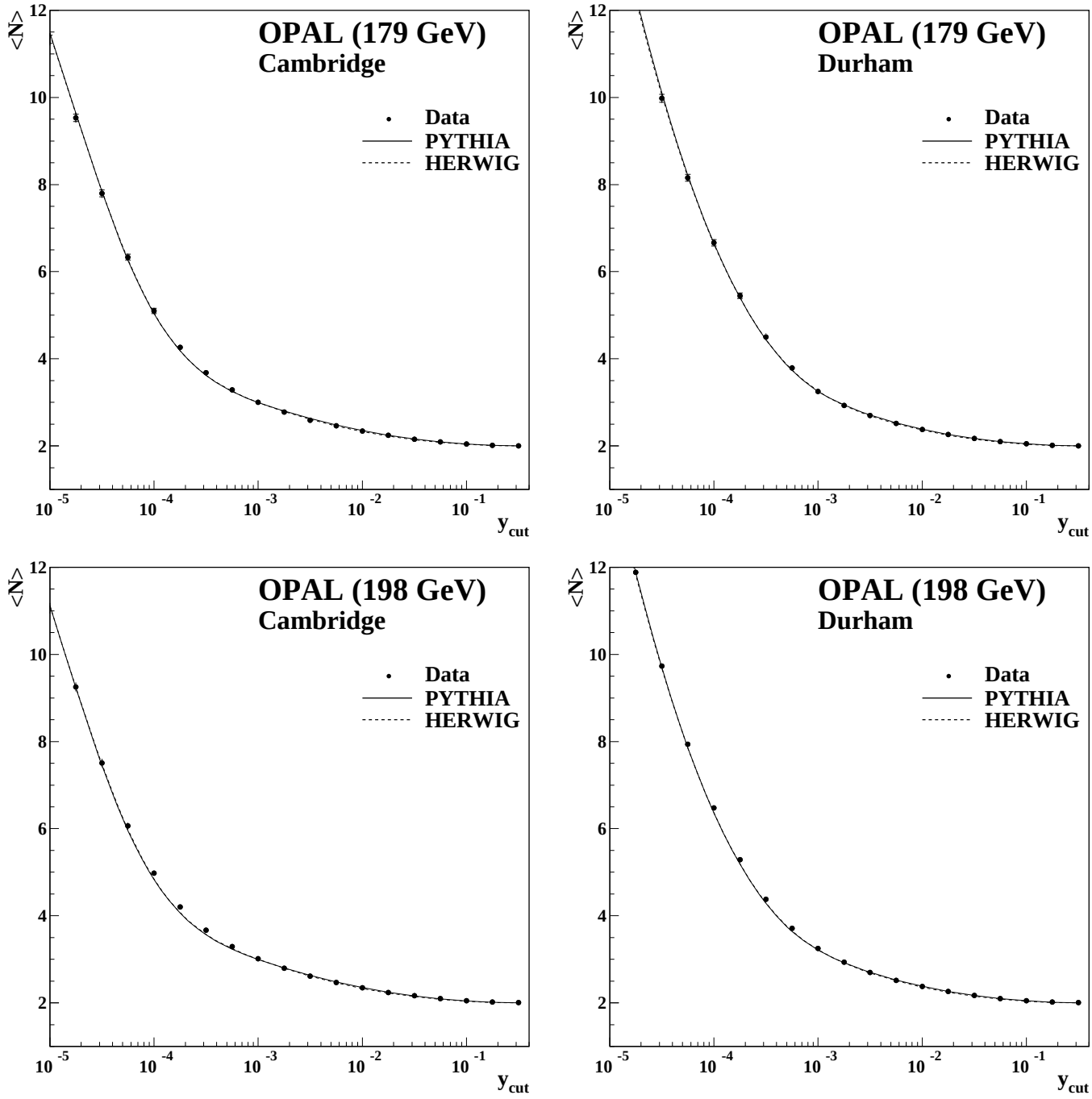


Figure 11: The average jet rates at the hadron level as a function of $y_{cut}$ for the Cambridge and Durham algorithms for two combined LEP2 datasets with $\sqrt{s} = 179$ GeV (top) and $\sqrt{s} = 198$ GeV (bottom). PYTHIA and HERWIG Monte Carlo expectations are represented by the curves. Error bars indicate total (statistical + systematic) errors.

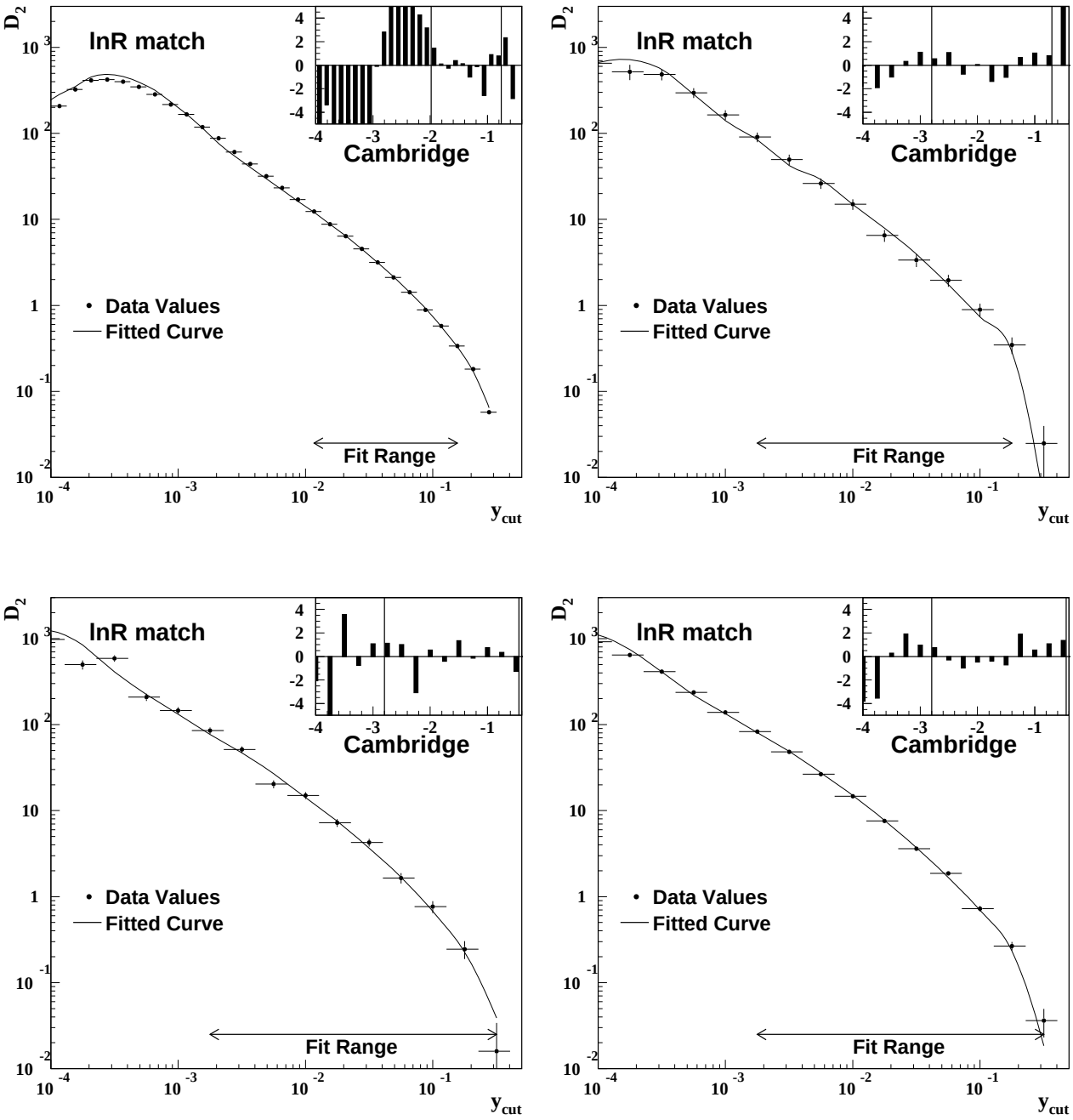


Figure 12: Fits of the parton level $D_2$ distribution using the Cambridge algorithm as a function of $y_{\rm cut}$ to the ln $R$ prediction for the 91 GeV (top left), 133 GeV (top right), 179 GeV (bottom left) and 198 GeV (bottom right) datasets. The inset plots show the pull of each point to the line of best fit and the two vertical lines delineate the fit range. Error bars represent statistical errors only.

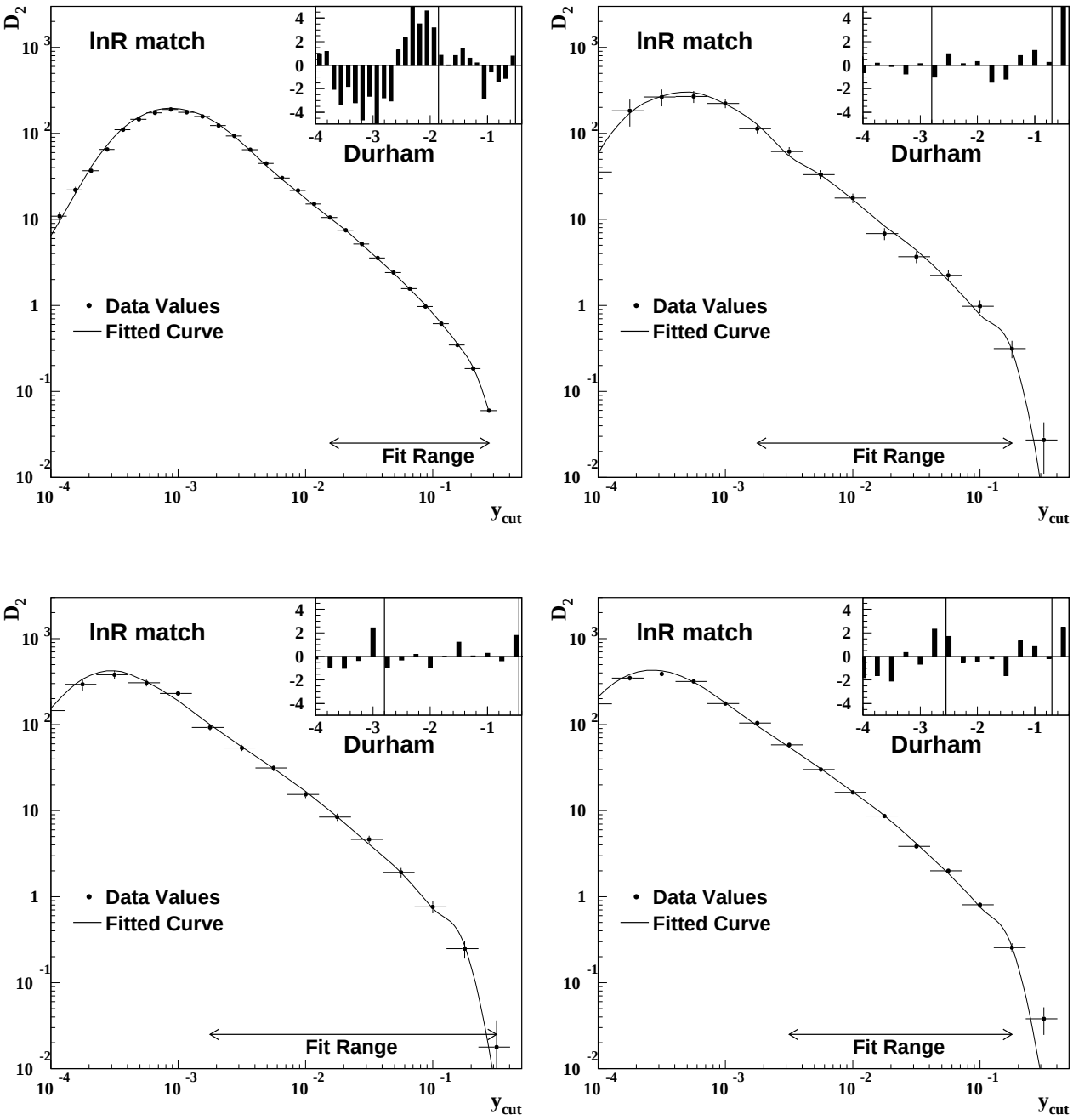


Figure 13: Fits of the parton level $D_2$ distribution using the Durham algorithm as a function of $y_{\rm cut}$ to the ln $R$ prediction for the 91 GeV (top left), 133 GeV (top right), 179 GeV (bottom left) and 198 GeV (bottom right) datasets. The inset plots show the pull of each point to the line of best fit and the two vertical lines delineate the fit range. Error bars represent statistical errors only.

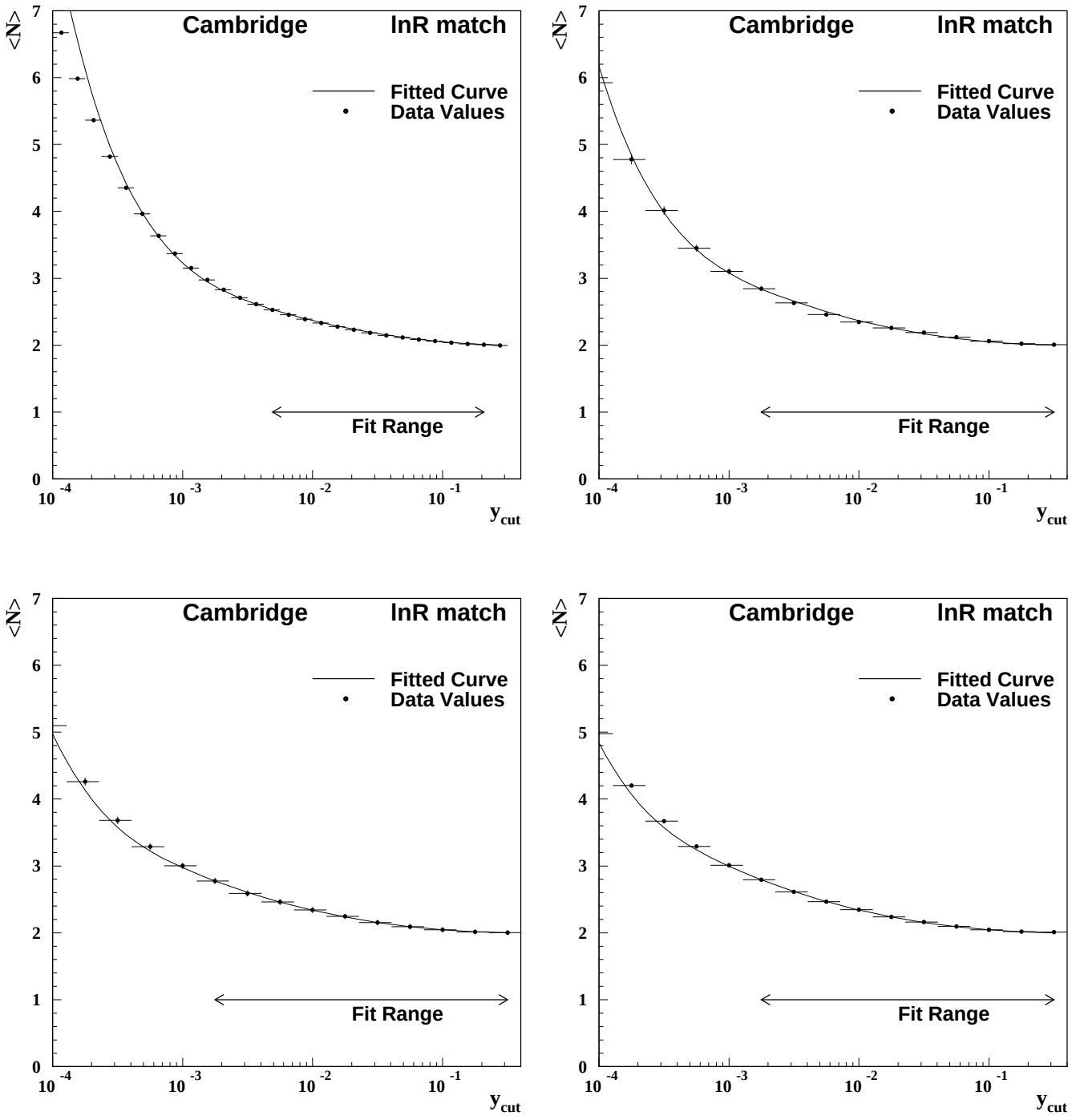


Figure 14: Fits of the parton level $\langle N \rangle$ distribution using the Cambridge algorithm as a function of $y_{\rm cut}$ to the ln $R$ prediction for the 91 GeV (top left), 133 GeV (top right), 179 GeV (bottom left) and 198 GeV (bottom right) datasets. Error bars represent statistical errors only.

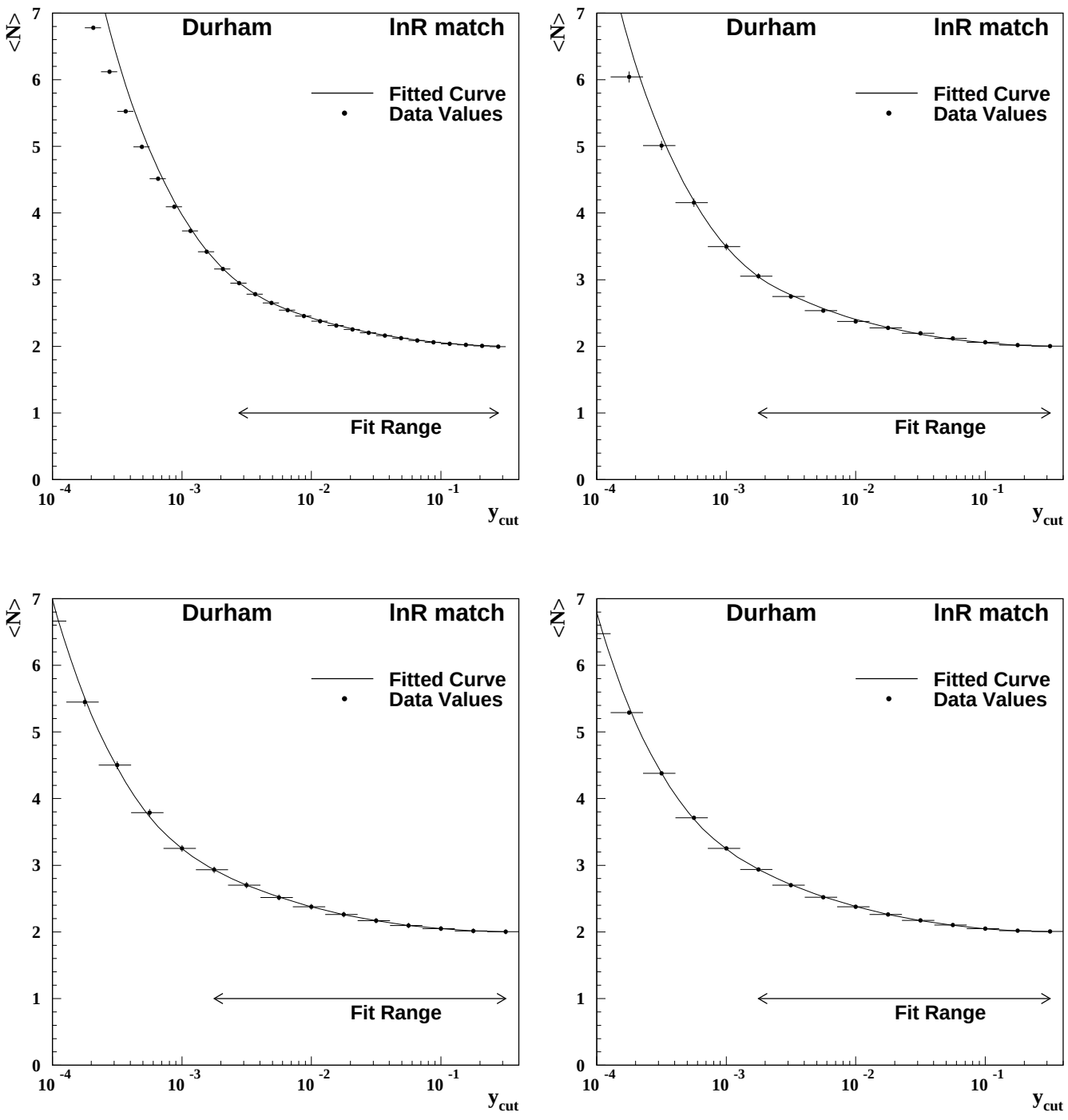


Figure 15: Fits of the parton level $\langle N \rangle$ distribution using the Durham algorithm as a function of $y_{\rm cut}$ to the ln $R$ prediction for the 91 GeV (top left), 130 GeV (top right), 189 GeV (bottom left) and 207 GeV (bottom right) datasets. Error bars represent statistical errors only.

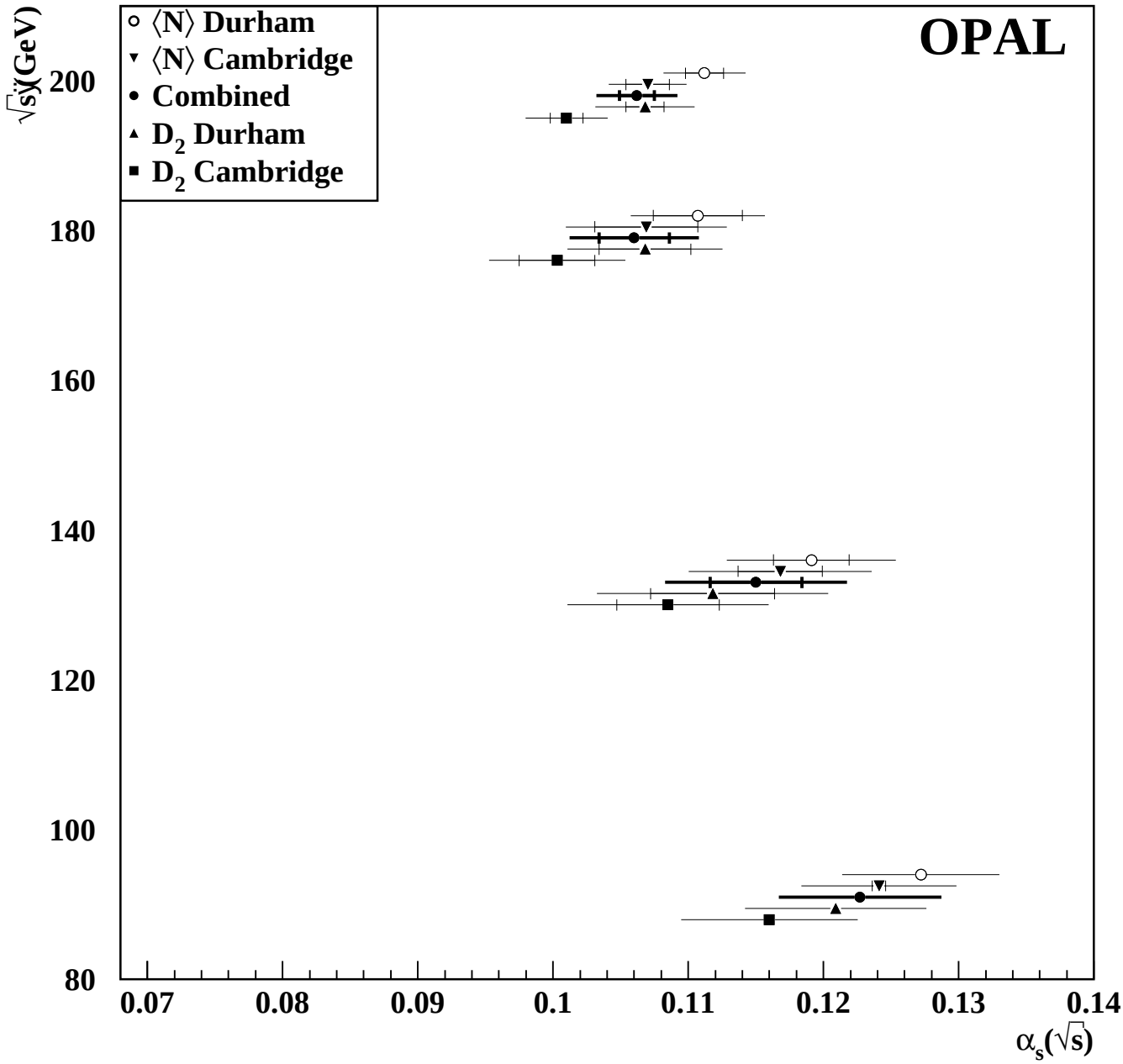


Figure 16: Comparison of combined $\alpha_{\rm s}$ values with those determined separately from the $D_2^D$, $D_2^C$, $\langle N\rangle^C$ and $\langle N\rangle^D$ distributions for each centre-of-mass energy dataset. Outer error bars indicate the size of the total errors while inner bars indicate the size of the statistical errors.

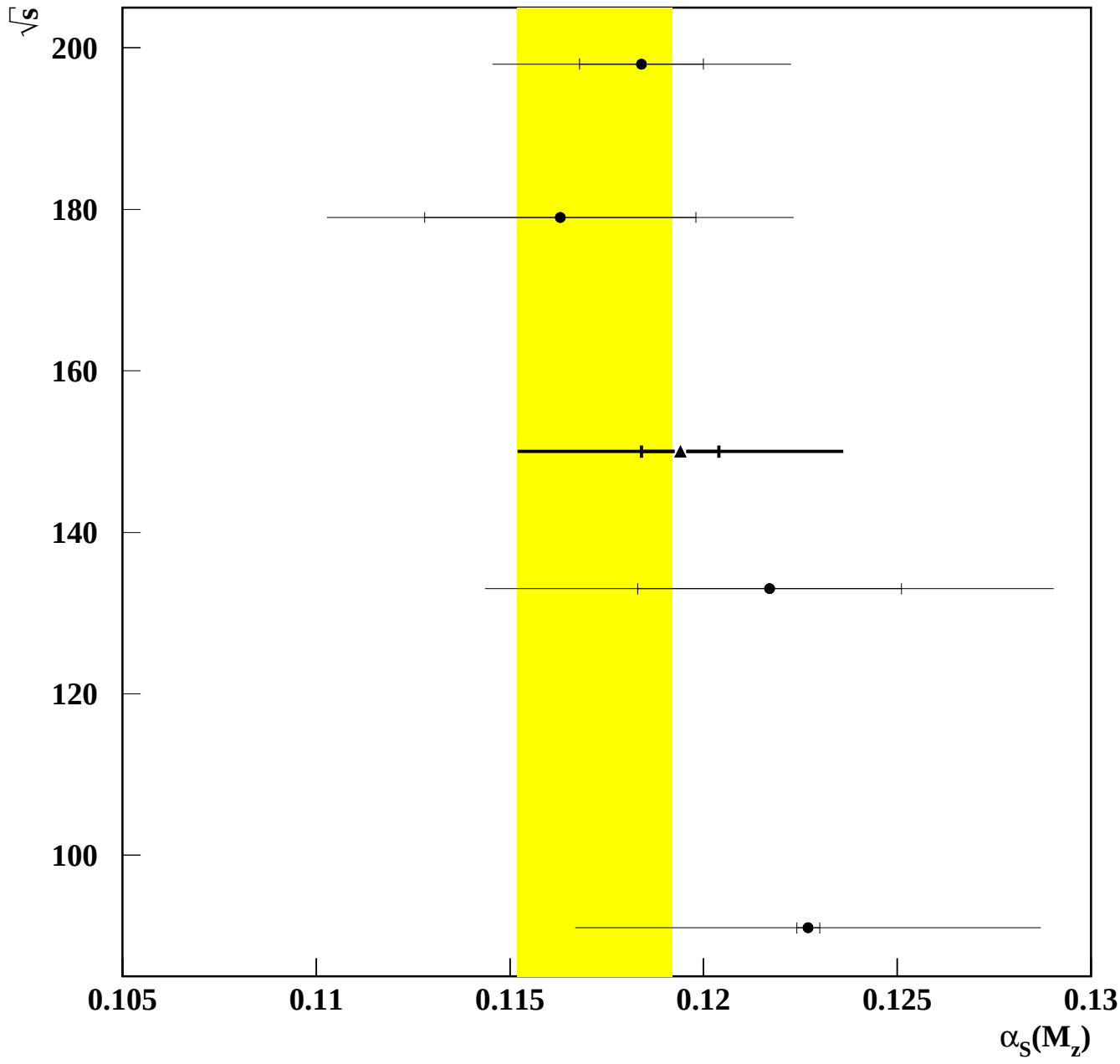


Figure 17: Comparison of the $\alpha_s$ values after having been run back to the $Z^0$ pole for each of the datasets. The bold point represents the value determined from the weighted mean of the four combined $\alpha_s(M_{Z^0})$ determinations. The shaded band corresponds to the one standard deviation range of the world average value of $\alpha_s(M_{Z^0})$ [42]. The inner error bars represent the statistical errors while the outer error bars represent the total error.

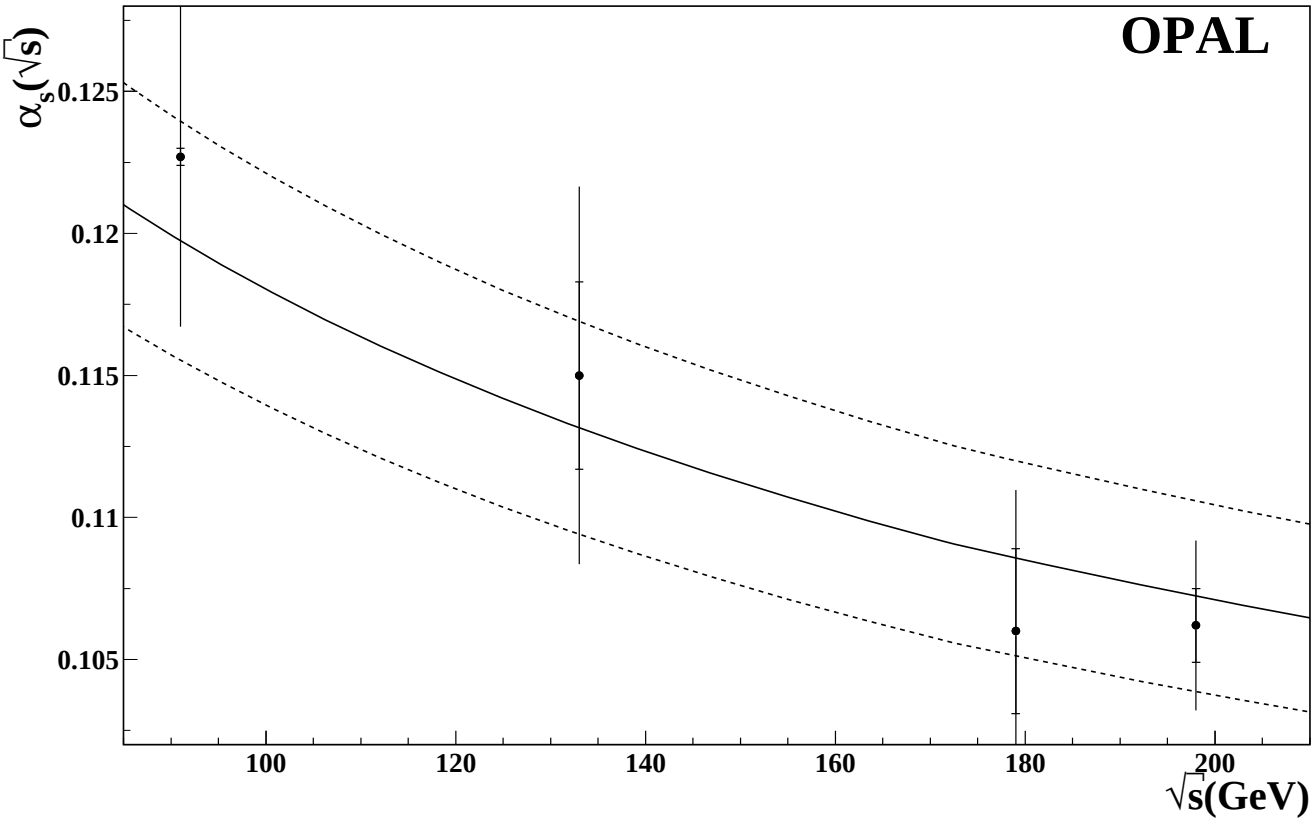


Figure 18: The running of $\alpha_s$ as a function of centre-of-mass energy. The points correspond to the $Z^0$-calibration dataset, the combined LEP1.5 data and the two LEP2 regions 161–183 and 189–207, respectively. The solid line corresponds to the expectation based on the weighted mean of the four combined $\alpha_s(M_{Z^0})$ determinations, and the outer dashed line to the total (statistical + systematic) uncertainty.